The Astrophysical Journal, 806:101 (23pp), 2015 June 10 doi:10.1088/0004-637X/806/1/101

LoCuSS: THE SLOW QUENCHING OF STAR FORMATION IN CLUSTER GALAXIES AND THE NEED FOR PRE-PROCESSING

C. P. Haines[1,2,3], M. J. Pereira[2], G. P. Smith[3], E. Egami[2], A. Babul[4], A. Finoguenov[5,6], F. Ziparo[3], S. L. McGee[3,7], T. D. Rawle[2,8], N. Okabe[9,11,12], and S. M. Moran[10]

[1] Departamento de Astronomía, Universidad de Chile, Casilla 36-D, Correo Central, Santiago, Chile; cphaines@das.uchile.cl
[2] Steward Observatory, University of Arizona, 933 North Cherry Avenue, Tucson, AZ 85721, USA
[3] School of Physics and Astronomy, University of Birmingham, Edgbaston, Birmingham, B15 2TT, UK
[4] Department of Physics and Astronomy, University of Victoria, 3800 Finnerty Road, Victoria, BC, V8P 1A1, Canada
[5] Department of Physics, University of Helsinki, Gustaf Hällströmin katu 2a, FI-0014 Helsinki, Finland
[6] Center for Space Science Technology, University of Maryland Baltimore County, 1000 Hilltop Circle, Baltimore, MD 21250, USA
[7] Leiden Observatory, Leiden University, P.O. Box 9513, NL-2300 RA Leiden, The Netherlands
[8] European Space Astronomy Centre, ESA, Villanueva de la Cañada, E-28691 Madrid, Spain
[9] Academia Sinica Institute of Astronomy and Astrophysics (ASIAA), P.O. Box 23-141, Taipei 10617, Taiwan
[10] Smithsonian Astrophysical Observatory, 60 Garden Street, Cambridge, MA 02138, USA
[11] Department of Physical Science, Hiroshima University, 1-3-1 Kagamiyama, Higashi-Hiroshima, Hiroshima 739-8526, Japan
[12] Kavli Institute for the Physics and Mathematics of the Universe (WPI), Todai Institutes for Advanced Study, University of Tokyo, 5-1-5 Kashiwanoha, Kashiwa, Chiba 277-8583, Japan
Received 2014 October 3; accepted 2015 April 15; published 2015 June 10

ABSTRACT

We present a study of the spatial distribution and kinematics of star-forming galaxies in 30 massive clusters at $0.15 < z < 0.30$, combining wide-field *Spitzer* 24 μm and *GALEX* near-ultraviolet imaging with highly complete spectroscopy of cluster members. The fraction ($f_{\rm SF}$) of star-forming cluster galaxies rises steadily with cluster-centric radius, increasing fivefold by $2r_{200}$, but remains well below field values even at $3r_{200}$. This suppression of star formation at large radii cannot be reproduced by models in which star formation is quenched in infalling field galaxies only once they pass within r_{200} of the cluster, but is consistent with some of them being first pre-processed within galaxy groups. Despite the increasing $f_{\rm SF}$-radius trend, the surface density of star-forming galaxies actually declines steadily with radius, falling ∼15× from the core to $2r_{200}$. This requires star formation to survive within recently accreted spirals for 2–3 Gyr to build up the apparent over-density of star-forming galaxies within clusters. The velocity dispersion profile of the star-forming galaxy population shows a sharp peak of 1.44 σ_v at $0.3r_{500}$, and is 10%–35% higher than that of the inactive cluster members at all cluster-centric radii, while their velocity distribution shows a flat, top-hat profile within r_{500}. All of these results are consistent with star-forming cluster galaxies being an infalling population, but one that must also survive ∼0.5–2 Gyr beyond passing within r_{200}. By comparing the observed distribution of star-forming galaxies in the stacked caustic diagram with predictions from the Millennium simulation, we obtain a best-fit model in which star formation rates decline exponentially on quenching timescales of 1.73 ± 0.25 Gyr upon accretion into the cluster.

Key words: galaxies: active – galaxies: clusters: general – galaxies: evolution – galaxies: stellar content

1. INTRODUCTION

The ability of galaxies to continuously form stars depends strongly on their global environment, with isolated central galaxies primarily evolving as star-forming spirals, while "red and dead" early-type galaxies completely dominate the cores of rich clusters, producing the SF-density or SF-radius relations (e.g., Kennicutt 1983; Lewis et al. 2002). Various physical mechanisms have been proposed over the years to remove (or consume) gas and quench star formation in spiral galaxies within massive clusters, such as ram-pressure or viscous stripping, starvation, harassment or tidal interactions (for reviews see, e.g., Boselli & Gavazzi 2006; Haines et al. 2007).

Clusters and their member galaxies, however, do not exist and evolve in isolation from the rest of the universe. In ΛCDM models structure formation occurs hierarchically, meaning that as the most massive collapsed structures in the universe, galaxy clusters form latest and are also the most dynamically immature (e.g., Boylan-Kolchin et al. 2009; Gao et al. 2012). Preferentially residing at the nodes of the complex filamentary web, they continually accrete dark matter (DM) halos hosting individual ∼L^* galaxies ($M_{\rm DM} \sim 10^{12}\,M_\odot$) or galaxy groups ($M_{\rm DM} \sim 10^{13-14}\,M_\odot$). The most massive clusters have on average doubled in mass since $z \sim 0.5$ (Boylan-Kolchin et al. 2009), while half of the galaxies in local clusters have been accreted since $z \sim 0.4$ (Berrier et al. 2009).

To correctly interpret the observed evolutionary and radial trends in cluster galaxy properties, it is thus fundamental to place them in this cosmological context whereby star-forming galaxies are being continually accreted into the clusters and transformed. Moreover, it is also vital to consider projection effects as many spectroscopic cluster members are actually infalling galaxies physically located outside the virial radius, and this contribution varies strongly with projected cluster-centric radius ($r_{\rm proj}$) and line of sight (LOS) velocity relative to the cluster redshift ($v_{\rm los} - \langle v \rangle$). This requires using cosmological simulations containing one or more massive clusters, and following the orbits and merger histories of the galaxies or sub-halos which are accreted into the cluster over time (e.g., Mamon et al. 2010). This approach gained early support when Balogh et al. (2000), Diaferio et al. (2001), and Ellingson et al. (2001) were able to reproduce the observed radial population gradients of star-forming galaxies in clusters in terms of galaxies on their first infall into the cluster.

The caustic diagram, which plots $v_{\rm los} - \langle v \rangle$ versus $r_{\rm proj}$, has been used to constrain the kinematics and accretion epochs of different cluster galaxy populations, as well as to constrain the masses, density profiles, and dynamical states of the clusters themselves (e.g., Moss & Dickens 1977; Binggeli et al. 1987; Biviano et al. 1997, 2013; Diaferio & Geller 1997; Diaferio 1999; Biviano & Katgert 2004; Gill et al. 2005; Serra et al. 2011; Mahajan et al. 2011; Hernández-Fernández et al. 2014; Muzzin et al. 2014; Jaffé et al. 2015).

This progress has permitted recent attempts to constrain the timescales required to halt star formation in recently accreted cluster spirals, with results supporting gentle physical mechanisms (e.g., starvation) that slowly quench star formation over a period of several Gyr (Wolf et al. 2009; von der Linden et al. 2010; De Lucia et al. 2012; Wetzel et al. 2013), rather than more violent processes (e.g., mergers) that rapidly terminate star formation (although see, e.g., Balogh et al. 2004; McGee et al. 2011; Wijesinghe et al. 2012).

In Haines et al. (2009) we estimated the composite radial population gradients in the fraction of star-forming galaxies ($f_{\rm SF}$) in 22 massive clusters at $0.15 < z < 0.30$ from the Local Cluster Substructure Survey (LoCuSS)[13] based on panoramic *Spitzer*/MIPS 24 μm data. A steady systematic increase in $f_{\rm SF}$ with cluster-centric radius was observed out to $\sim r_{200}$, similar to those found previously (Ellingson et al. 2001; Lewis et al. 2002; Weinmann et al. 2006). Through comparison with galaxies infalling and orbiting around massive clusters ($M_{200} \gtrsim 10^{15} M_{\odot}$) from the Millennium Simulation (Springel et al. 2005), it was possible to approximately reproduce the radial population trends in the context of a simple infall model, in which star-forming field galaxies are accreted into the cluster and their star formation rapidly quenched upon their first pericenter. The key limitation of this work was the lack of redshifts to identify cluster galaxies, such that we had to statistically account for the contamination for field galaxy interlopers when estimating the $f_{\rm SF}(r)$.

We have since completed Arizona Cluster Redshift Survey (ACReS)[14], which provides highly complete spectroscopy of cluster members for all 30 clusters from LoCuSS[15] with wide-field *Spitzer*/MIPS data. With this data, Haines et al. (2013) found the specific star formation rates (sSFRs) of massive ($\mathcal{M} \gtrsim 10^{10} M_{\odot}$) star-forming cluster galaxies within r_{200} to be systematically 28% lower than their counterparts in the field at fixed stellar mass and redshift, a difference significant at the 8.7σ level. This is the unambiguous signature of star formation in most (and possibly all) massive star-forming galaxies being slowly quenched upon accretion into clusters, and was best fit by models in which their star formation rates (SFRs) decline exponentially on quenching timescales in the range 0.7–2.0 Gyr.

In this article we analyze the spatial distribution and kinematics of star-forming galaxies within the same set of 30 clusters, and by comparing with predictions from cosmological simulations, draw further independent constraints on the quenching timescale. In particular, we determine the radial surface density profile, $\Sigma(r)$, of star-forming cluster galaxies and show that it declines steadily with radius, falling $\sim$15× from the core to $2r_{200}$. We show that this simple observation provides powerful constraints for how long massive star-forming galaxies are able to continue forming stars once they are accreted into rich clusters, quickly ruling out models in which star formation is rapidly halted in infalling spirals when they pass within r_{200}. We also re-examine the radial population gradients of star-forming galaxies ($f_{\rm SF}$-radius relation) out to $3r_{200}$, where we find a shortfall of star-forming galaxies in comparison to the coeval field population that cannot be easily explained by purely cluster-related quenching mechanisms, indicating a need for galaxies to be first pre-processed within infalling galaxy groups.

In Section 2 we present our observational data, and in Section 3 the main results. In Section 4 we follow the infall and orbits of galaxies in the vicinity of massive galaxy clusters from the Millennium simulation, to predict their spatial distributions and kinematics as a function of accretion epoch. These model predictions are then compared to observations in Section 5. We discuss the resultant constraints on the timescales required to quench star formation in recently accreted galaxies and the need for pre-processing in Section 6 and summarize in Section 7. Throughout we assume $\Omega_M = 0.3$, $\Omega_\Lambda = 0.7$ and $H_0 = 70$ km s^{-1} Mpc^{-1}.

2. DATA

LoCuSS is a multi-wavelength survey of X-ray luminous galaxy clusters at $0.15 \leqslant z \leqslant 0.3$ (Smith et al. 2010a) drawn from the *ROSAT* All Sky Survey cluster catalogs (Böhringer et al. 2004). The first 30 clusters from our survey benefit from a particularly rich dataset, including: Subaru/Suprime-Cam optical imaging (Okabe et al. 2010), *Spitzer*/MIPS 24 μm maps, *Herschel*/PACS+SPIRE 100–500 μm maps, *Chandra* and/or *XMM* X-ray data, *GALEX* UV data, and near-infrared (NIR) imaging. All of these data embrace at least $25' \times 25'$ fields of view centered on each cluster, and thus probe them out to 1–2 virial radii (Haines et al. 2010; Pereira et al. 2010; Smith et al. 2010b). These 30 clusters were selected from the parent sample simply on the basis of being observable by Subaru on the nights allocated to us (Okabe et al. 2010), and should therefore not suffer any gross biases toward (for example) cool core clusters, merging clusters, etc. Indeed, Okabe et al. (2010) show that the sample is statistically indistinguishable from a volume-limited sample.

2.1. Chandra/XMM X-ray Imaging

All but two (Abell 291, Abell 2345) of the 30 clusters have available deep *Chandra* data ($t_{\rm exp}$ = 9–120 ks). Deprojected DM densities, gas densities, and gas temperature profiles for each cluster were derived by fitting the phenomenological cluster models of Ascasibar & Diego (2008) to a series of annular spectra extracted for each cluster (Sanderson & Ponman 2010). The best-fitting cluster models were then used to estimate r_{500}, the radius enclosing a mean overdensity of 500 with respect to the critical density of the universe at the cluster redshift (Sanderson et al. 2009).

The r_{500} value for Abell 689 is taken from Giles et al. (2012), as they separated the extended cluster X-ray emission from the central BL Lac, and for the clusters lacking *Chandra* data, the r_{500} values are taken from the *XMM* analysis of Martino et al. (2014). For the 23 clusters in common with the joint *Chandra–XMM* analysis of the LoCuSS high-L_X cluster sample of Martino et al. (2014), there is good consistency of the cluster radii with $\langle r_{500,\rm Haines}/r_{500,\rm Martino} \rangle = 1.003 \pm 0.034$.

[13] http://www.sr.bham.ac.uk/locuss/
[14] http://herschel.as.arizona.edu/acres/acres.html
[15] http://herschel.as.arizona.edu/locuss/locuss.html

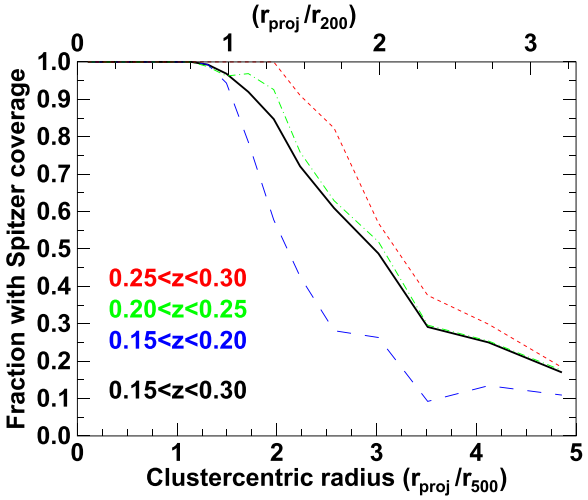

Figure 1. Radial coverage of the *Spitzer* /MIPS 24 μm data. Each curve shows the fraction of cluster members covered by our 24 μm images (25′ × 25′ field of view) as a function of cluster-centric radius in units of r_{500}, for clusters in the following redshift ranges: $0.15 < z < 0.20$ (long-dashed blue curves); $0.20 < z < 0.25$ (dotted–dashed green curves); $0.25 < z < 0.30$ (short-dashed red curves); $0.15 < z < 0.30$ (solid black curves).

The *Chandra* data were also used to identify X-ray active galactic nucle: (AGNs) as described in Haines et al. (2012). The survey limit of six broad (0.3–7 keV) X-ray counts results in on-axis sensitivity limits of $L_X \leqslant 1.0 \times 10^{42}$ erg s^{-1} for X-ray AGNs, at the cluster redshift for all 28 systems (Table 1 from Haines et al. 2012).

Deep *XMM* data was available for 23 systems, allowing other groups and clusters in the region to be identified. Each 0.5–2 keV image is decomposed into unresolved and extended emission, following the wavelet technique of Finoguenov et al. (2009). For each extended source, we attempt to identify the redshift of its associated group/cluster by examining the Subaru optical images for likely BCGs near the center of the X-ray emission and/or groups of galaxies with similar redshifts from ACReS within the X-ray contours.

2.2. Mid-infrared Observations

All 30 clusters were observed at 24 μm with MIPS (Rieke et al. 2004) on board the *Spitzer Space Telescope* (*SST*)[16] (PID: 40872; PI: G.P. Smith). The resulting 24 μm mosaics were analyzed with SExtractor (Bertin & Arnouts 1996), producing catalogs which are on average 90% complete to 400 μJy.

Each cluster was observed across a fixed 25′ × 25′ field of view, resulting in the clusters being covered out to different cluster-centric radii in units of r_{500}, depending on their redshift and r_{500} radius, as well as the orientation of the *Spitzer* images. Figure 1 shows that we probe out to larger cluster-centric radii for the highest redshift clusters ($0.25 < z < 0.30$) than those in our lowest redshift bin ($0.15 < z < 0.20$). Averaging over the full redshift range (0.15–0.30; solid black curve), our 24 μm coverage is essentially complete out to r_{200}, falling to ∼45% at $2r_{200}$, based on the conversion $r_{500} = 0.66 r_{200}$ (Sanderson & Ponman 2003).

[16] This work is based in part on observations made with the *SST*, which is operated by the Jet Propulsion Laboratory, California Institute of Technology under a contract with NASA (contract 1407).

2.3. UV, Optical, and NIR Data

Wide-field *J*- and *K*-band NIR imaging was obtained for all 30 clusters using either WFCAM on the 3.8 m United Kingdom Infrared Telescope (UKIRT)[17] (52′ × 52′ field of view; 26/30 clusters) or NEWFIRM on the 4.0 m Mayall telescope at Kitt Peak[18] (27′ × 27′; 4/30 clusters), in each case reaching depths of $K \sim 19$, $J \sim 21$.

Wide-field deep UV imaging from the *GALEX* satellite was obtained for 26/30 clusters, primarily through the Cycle 4 (GI4-090; PI. G. P. Smith) and Cycle 6 (GI6-046; PI. S. Moran) Guest Investigator Programs. The Cycle 4 program provided far-ultraviolet (FUV) and near-ultraviolet (NUV) imaging for 14 clusters ($t_{\rm exp} = 3.2$–13.6 ks), while comparable FUV+NUV data were obtained for 7 more clusters ($t_{\rm exp} = 3.4$–29.0 ks) from the *GALEX* science archive. Sixteen clusters were observed in Cycle 6, including 8 systems not previously observed, but this provided only deep NUV imaging ($t_{\rm exp} = 2.9$–36.3 ks), the operations of the FUV camera having previously been suspended. The *GALEX* instrument has a circular field of view of radius 0.55 deg, ensuring full ultraviolet coverage for galaxies in our NIR WFCAM fields. The total NUV exposure times and 5σ magnitude limits, after correcting for Galactic extinction as in Wyder et al. (2007), are shown in Table 1.

Optical photometry in the *ugriz* bands was taken from the Sloan Digital Sky Survey, using the dereddened SDSS model magnitudes. Twenty-six of the 30 clusters lie within the DR-10 footprint, while 23 have both SDSS *ugriz* and deep *GALEX* NUV photometry, allowing star-forming galaxies to be identified from their blue NUV–*r* colors.

2.4. MMT/Hectospec Spectroscopy

We have recently completed ACReS (M. J. Pereira et al. 2015, in preparation) a long-term spectroscopic programme to observe our sample of 30 galaxy clusters with MMT/Hectospec. Target galaxies are primarily *K*-band selected down to a limit of $m_K^*(z_{\rm cl}) + 1.5$ or fainter (depending on the number of targets produced), to produce an approximately stellar mass-limited sample down to $\mathcal{M} \sim 2 \times 10^{10}\, M_\odot$. Higher priorities are given to target galaxies also detected at 24 μm to obtain a virtually complete census of obscured star formation in the cluster population. Further details of the survey aims and targeting strategy are given in Haines et al. (2013). Eleven of our 30 clusters were also observed by the Hectospec Cluster Survey (Rines et al. 2013), providing redshifts for an additional 971 cluster members. Redshifts for a further 112, 92, and 49 members of clusters RXJ1720.1+2638, Abell 383, and Abell 209 are included from Owers et al. (2011), Geller et al. (2014), and Mercurio et al. (2003) respectively. Table 1 lists the number of spectroscopic members for each cluster, with the contributions taken from other published surveys indicated in parentheses, giving us a grand total of 10,950 cluster members with redshifts. Averaging over all 30 systems, we achieve spectroscopic completeness levels of 66% for $M_K < -23.10$ ($M_K^* + 1.5$) cluster galaxies across the full WFCAM/

[17] UKIRT is operated by the Joint Astronomy Centre on behalf of the Science and Technology Facilities Council of the United Kingdom.

[18] Kitt Peak National Observatory, National Optical Astronomy Observatory, which is operated by the Association of Universities for Research in Astronomy under cooperative agreement with the National Science Foundation.

Table 1
The Cluster Sample

Cluster Name	$\langle z \rangle$	N_z (lit)	r_{500} (Mpc)	M_{500} ($10^{14}\,M_\odot$)	σ_v (km s^{-1})	$t_{\rm exp}$(NUV) (s)	$m_{\rm AB}$(NUV) (S/N = 5)
Abell 68	0.2510	194(0)	0.955	3.193	1186^{+89}_{-88}	6731	22.90
Abell 115	0.1919	213(36)	1.304	7.628	1219^{+72}_{-71}	16217	23.36
Abell 209	0.2092	393(49)[c]	1.230	6.519	1369^{+65}_{-67}	11616	23.76
Abell 267	0.2289	230(139)[a]	0.994	3.515	1045^{+52}_{-52}	11268	23.32
Abell 291	0.1955	126(0)	0.868[e]	2.259	704^{+80}_{-82}	6059	23.16
Abell 383	0.1887	266(92)[d]	1.049	3.958	950^{+64}_{-63}	6117	23.16
Abell 586	0.1707	247(21)	1.150	5.117	933^{+55}_{-54}	…	…
Abell 611	0.2864	297(7)	1.372	9.847	1039^{+67}_{-67}	9928	23.01
Abell 665	0.1827	359(31)	1.381	8.975	1227^{+59}_{-59}	9503	23.26
Abell 689	0.2776	338(153)[a]	1.126[f]	5.390	721^{+57}_{-58}	…	…
Abell 697	0.2821	486(141)[a]	1.505	12.93	1268^{+57}_{-58}	36858	23.89
Abell 963	0.2043	466(50)[a]	1.275	7.226	1119^{+49}_{-49}	29043	23.96
Abell 1689	0.1851	857(416)[a]	1.501	11.55	1541^{+46}_{-46}	7716	23.34
Abell 1758	0.2775	471(50)[a]	1.376	9.835	1442^{+64}_{-63}	20977	23.88
Abell 1763	0.2323	423(126)[a]	1.220	6.522	1358^{+52}_{-53}	13589	23.80
Abell 1835	0.2524	1083(608)[a]	1.589	14.73	1485^{+35}_{-35}	21827	23.50
Abell 1914	0.1671	454(65)[a]	1.560	12.73	1055^{+44}_{-44}	3804	23.17
Abell 2218	0.1733	342(49)	1.258	6.716	1245^{+42}_{-42}	14617	23.73
Abell 2219	0.2257	628(297)[a]	1.494	11.90	1332^{+59}_{-58}	9886	23.42
Abell 2345	0.1781	405(39)	1.249[e]	6.607	1000^{+43}_{-43}	9864	23.49
Abell 2390	0.2291	517(140)	1.503	12.16	1372^{+63}_{-62}	6819	22.35
Abell 2485	0.2476	196(0)	0.830	2.088	799^{+54}_{-54}	…	…
RXJ0142.0+2131	0.2771	204(15)	1.136	5.531	1123^{+66}_{-63}	…	…
RXJ1720.1+2638	0.1599	473(114)[b]	1.530	11.92	938^{+37}_{-36}	3074	22.67
RXJ2129.6+0005	0.2337	334(78)[a]	1.227	6.648	879^{+82}_{-82}	36323	23.72
ZwCl0104.4+0048 (Z348)	0.2526	185(1)	0.760[e]	1.613	806^{+74}_{-73}	14435	23.46
ZwCl0823.2+0425 (Z1693)	0.2261	337(4)	1.050	4.130	671^{+50}_{-48}	14314	23.41
ZwCl0839.9+2937 (Z1883)	0.1931	173(3)	1.107	4.674	834^{+89}_{-87}	21250	23.39
ZwCl0857.9+2107 (Z2089)	0.2344	147(0)	1.024	3.866	815^{+79}_{-80}	20225	23.68
ZwCl1454.8+2233 (Z7160)	0.2565	157(1)	1.128	5.294	988^{+84}_{-84}	19850	23.58

Note. Column (1) cluster name; column (2) mean redshift of cluster members; column (3) total number of spectroscopic cluster members (contribution taken from the literature, including new redshifts from Rines et al. 2013[a]; Owers et al. 2011[b]; Mercurio et al. 2003[c] and Geller et al. 2014[d]); column (4) radius r_{500} in Mpc. [e]From Martino et al. (2014), [f]from Giles et al. (2012); column (5) cluster mass M_{500} in $10^{14}\,M_\odot$; column (6) velocity dispersion of cluster members within r_{200}; column (7) total exposure time of *GALEX* NUV images; column (8) NUV magnitude limit for S/N = 5.

NEWFIRM fields, rising to 80% for those galaxies with *Spitzer* coverage and 96% for those detected at 24 μm.

The likelihood that a given galaxy was targeted for spectroscopy depends strongly on both its location with respect to the cluster center as well as its photometric properties (K-band magnitude, J–K color, 24 μm flux), as detailed in Haines et al. (2013). To account for this, each galaxy is weighted by the inverse probability of it having being observed spectroscopically, following the approach of Norberg et al. (2002).

2.5. Identification of Cluster Members and Field Galaxy Samples

Members of each cluster are identified from the redshift versus projected cluster-centric radius plot as lying within the "trumpet"-shaped caustic profile expected for galaxies infalling and subsequently orbiting within a massive virialized structure (Diaferio & Geller 1997; Geller 1999; Dünner et al. 2007). For most systems, there is a strong contrast in phase-space density from inside to outside these caustics (Rines & Diaferio 2006), making their visual identification relatively simple. The central redshift $\langle z \rangle$ and velocity dispersion σ_v of each cluster (Table 1) are iteratively measured for member galaxies within r_{200} (estimated as in Finn et al. 2008), using the biweight scale estimator ($S_{\rm BI}$; Beers et al. 1990), with uncertainties estimated using bootstrap resampling.

The field galaxy sample was taken from the same data set as the primary cluster galaxy sample, but was located in narrow redshift ranges on either side of the cluster, for which our spectroscopic survey ACReS should still be complete to $M_K^* + 1.5$ (for full details see Haines et al. 2013). Overall, 1398 coeval ($0.15 < z < 0.30$) field galaxies with $M_K < M_K^* + 1.5$ and 24 μm coverage were identified within these narrow redshift slices on either side of the clusters (699 in front, 699 behind), after excluding regions where other X-ray galaxy groups had been previously detected from our *XMM* data.

2.6. Stellar Masses and SFRs

Rest-frame UV–optical colors and absolute magnitudes were determined using the k-corrections of Chilingarian et al. (2010). Stellar masses ($\mathcal{M}$) were estimated from the K-band luminosities using the linear relation between K-band stellar

mass-to-light ratio and rest-frame g–i color from Bell et al. (2003), adjusted by −0.15 dex to be valid for a Kroupa (2002) IMF. Where SDSS photometry was unavailable we classified the galaxy as being either star-forming or passive according to whether it was 24 μm or NUV detected or not, and adopted appropriate mass-to-light ratios.

For each 24 μm-detected galaxy with known redshift, its intrinsic bolometric luminosity ($L_{\rm TIR}$) and rest-frame 24 μm luminosity is estimated by comparison of its 24 μm flux to the luminosity-dependent template infrared spectral energy distributions (SEDs) of Rieke et al. (2009). The latter is then converted to an obscured SFR using the calibration of Rieke et al. (2009)

$$\mathrm{SFR_{IR}}\left(M_\odot\ \mathrm{yr}^{-1}\right) = 7.8\times10^{-10}\,L\left(24\,\mu\mathrm{m},\,L_\odot\right), \qquad (1)$$

which is valid for either a Kroupa (2002) or Chabrier (2003) IMF. Our *Spitzer* data should be sensitive to galaxies with ongoing obscured star formation occuring at rates down to 2.0 $M_\odot$ yr^{-1} in our most distant clusters ($z\sim0.28$).

Local quiescent early-type galaxies are known to emit in the mid-infrared at levels much higher than expected from photospheric emission alone (Clemens et al. 2009). This excess at 10–30 μm has been shown to be due to silicate emission from the dusty circumstellar envelopes of mass-losing evolved AGB stars (Bressan et al. 2006) rather than residual ongoing star formation. We may thus worry that some of our cluster galaxies may be mistakenly classed as star-forming due to 24 μm emission coming from TP-AGB stars.

The SEDs of evolved stellar populations including emission from dusty circumstellar envelopes peak at 10–20 μm, but then drop rapidly at longer wavelengths (Piovan et al. 2003), so galaxies whose 24 μm emission is due to TP-AGB stars should not be detected in our *Herschel*/PACS data, unlike normal star-forming galaxies whose infrared SEDs peak at 70–170 μm (e.g., Dale et al. 2012). For the 11 nearest clusters ($0.15<z<0.20$) in our sample, >98% of galaxies with $\mathrm{SFR_{IR}}>2.0\,M_\odot$ yr^{-1} and *Herschel*/PACS coverage were also detected at 100 μm, while >99% show clear Hα emission in our ACReS MMT/Hectospec spectra, indicating that their 24 μm emission is indeed due to ongoing star formation.

In a comparable *Spitzer*/MIPS analysis of 814 galaxies in the Shapley supercluster at $z=0.048$, sensitive to much lower obscured SFRs ($\mathrm{SFR_{IR}}\sim0.05M_\odot$ yr^{-1}) Haines et al. (2011b) did find a significant population of quiescent (based upon a lack of Hα emission) cluster galaxies detected at 24 μm, but none with 24 μm luminosities that would convert to an obscured SFR above $0.5\,M_\odot$ yr^{-1}. They also obtained a tight correlation (0.22 dex) between the 24 μm and the 1.4 GHz radio luminosities for star-forming cluster galaxies, down to $\mathrm{SFR_{IR}}\sim1.0\,M_\odot$ yr^{-1}, consistent with both the mid-infrared and radio emission being due to star formation.

3. RESULTS

3.1. Radial Population Gradients

Figure 2 shows the fraction of massive ($\mathcal{M}>2.0\times10^{10}\,M_\odot$) cluster galaxies with obscured star formation occurring at rates $\mathrm{SFR_{IR}}>2.0\,M_\odot$ yr^{-1} ($f_{\rm SF}$) as a function of projected cluster-centric radius in units of r_{500}, across the full sample of 30 clusters. The fractions only consider cluster members covered by the *Spitzer* 24 μm maps, and exclude X-ray AGNs and QSOs, as their 24 μm emission is usually dominated by dust heated by the active nucleus rather than star formation (e.g., Xu et al. 2015). BCGs are also excluded due to their unique evolutions (Lin & Mohr 2004), and the direct link between BCG activity and the presence of cooling flows within clusters (Smith et al. 2010a; Rawle et al. 2012).

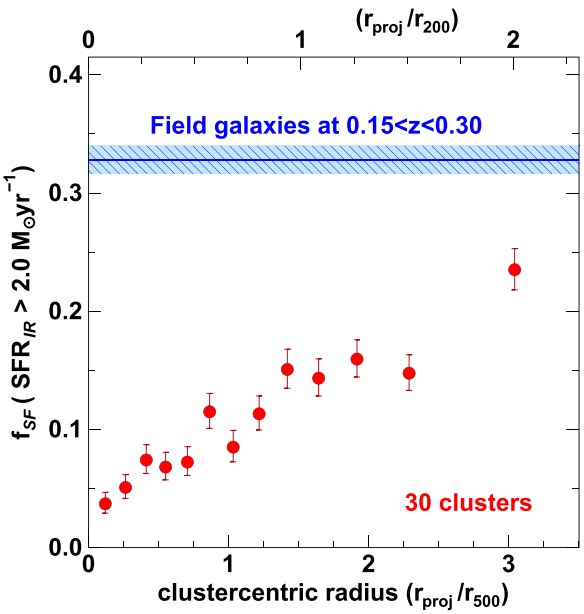

Figure 2. Radial population gradients for MIR-selected star-forming galaxies from our stacked sample of 30 clusters. Red symbols show the fraction of massive ($\mathcal{M}>2.0\times10^{10}\,M_\odot$) cluster galaxies with obscured star formation at rates $\mathrm{SFR_{IR}}>2.0\,M_\odot$ yr^{-1} as a function of projected cluster-centric radius ($r_{\rm proj}/r_{500}$). The error bars indicate the uncertainties derived from binomial statistics calculated using the formulae of Gehrels (1986). Each radial bin contains 400 cluster galaxies. The blue horizontal line indicates the corresponding fraction of field galaxies ($\mathcal{M}>2.0\times10^{10}\,M_\odot$; $0.15<z<0.30$) with $\mathrm{SFR_{IR}}>2.0\,M_\odot$ yr^{-1} and its 1σ confidence limits (shaded region).

The fraction of obscured star-forming galaxies increases steadily with cluster-centric radius from $f_{\rm SF}\sim0.04$ in the cluster core to $f_{\rm SF}\sim0.23$ at $3.0r_{500}$ ($1.9r_{200}$). However, even at these large radii the $f_{\rm SF}$ remains well (∼1/3) below that seen in coeval field galaxies ($f_{\rm SF}=0.33\pm0.01$; blue line). A simple linear extrapolation of the observed trend suggests that the $f_{\rm SF}$ should reach that of the field galaxy population at $\sim4.5r_{500}$. However, the limited extents of our *Spitzer* 24 μm maps mean that we cannot establish whether this occurs or not.

The fraction of star-forming cluster galaxies evolves very rapidly at these redshifts, with $f_{\rm SF}\propto(1+z)^{7.6\pm1.1}$ (Haines et al. 2013). It is thus vital to ensure that this shortfall in star-forming cluster galaxies at large radii with respect to field values is not produced by a redshift bias between the two samples. This is certainly not the case here, as the mean redshifts of each radial bin for the cluster populations all lie in the range 0.217–0.241, while for the field population $\langle z\rangle=0.225$. There is a marginal redshift bias within our cluster sample, as the outer two radial bins have $\langle z\rangle=0.241$, while the remaining bins all have mean redshifts in the range 0.217–0.231. This is due to our *Spitzer* data providing wider radial coverage (in terms of r_{500}) for the higher redshift systems, but it is likely only a marginal effect, artificially increasing the outer two $f_{\rm SF}$ by $\lesssim$10% (or ∼0.02 in the figure).

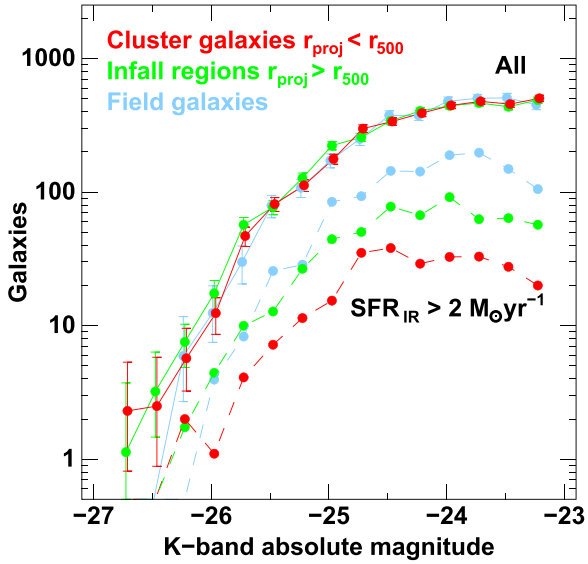

Figure 3. *K*-band luminosity functions (LFs) for cluster galaxies within r_{500} (red solid curve), galaxies from the infall regions ($r_{proj} > r_{500}$; green solid curve) and the coeval field population (light-blue solid curve). The latter two are normalized to contain the same total number of $M_K < -23.1$ galaxies as the cluster galaxy population, and the points are slightly shifted horizontally to permit easier comparison of the LFs. Error bars indicate Poissonian uncertaintes based on Gehrels (1986). The corresponding *K*-band LFs for star-forming galaxies with $SFR_{IR} > 2.0\ M_\odot\ yr^{-1}$ are indicated by dashed curves.

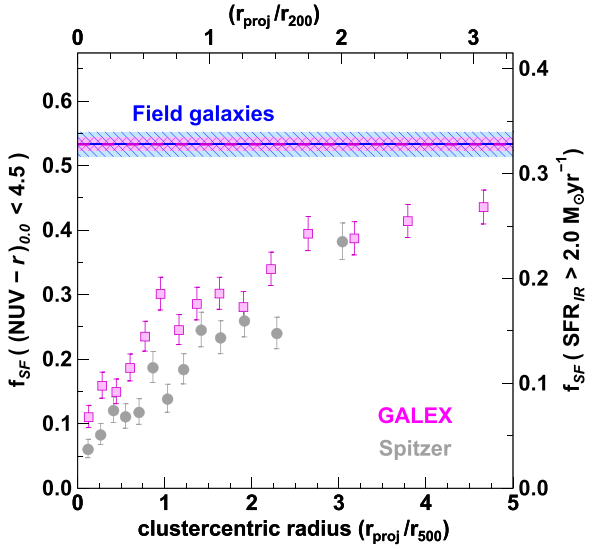

Figure 4. Comparison of radial population gradients for star-forming cluster galaxies selected in the ultraviolet and mid-infrared. Magenta squares show the fraction of massive ($\mathcal{M} > 2.0 \times 10^{10}\ M_\odot$) cluster galaxies with blue rest-frame UV–optical colors, $(NUV-r)_{0.0} < 4.5$, indicating ongoing unobscured star formation. Each radial bin contains 300 cluster galaxies. The magenta dashed line indicates the corresponding fraction of field galaxies ($\mathcal{M} > 2.0 \times 10^{10}\ M_\odot$; $0.15 < z < 0.30$) with $(NUV-r)_{0.0} < 4.5$ and its 1σ confidence levels (magenta shaded region). Gray symbols show the corresponding fractions of cluster galaxies with $SFR_{IR} > 2.0\ M_\odot\ yr^{-1}$ taken from Figure 2, scaled via the right-hand axis such that the fraction of field galaxies with $SFR_{IR} > 2.0\ M_\odot\ yr^{-1}$ (blue dashed line) coincides with the corresponding fraction selected in the NUV.

A second possible explanation for the lower f_{SF} among cluster galaxies would be if they were more massive on average than the field galaxy comparison sample, as f_{SF} is known to decline with increasing stellar mass at fixed galaxy density (e.g., Haines et al. 2007). However, the mean stellar masses of cluster galaxies for each radial bin in Figure 2 are always within 0.04 dex of that of the coeval field population. Moreover, the *K*-band luminosity functions of cluster galaxies within r_{500} (excluding BCGs), those in the infall regions ($r_{proj} > r_{500}$), and the field galaxy samples are all indistinguishable (Figure 3). We also note that due to the fixed SFR lower limit of $2.0\ M_\odot\ yr^{-1}$ used to define a star-forming galaxy, the f_{SF} do not vary much with stellar mass (*K*-band luminosity). We therefore exclude secular quenching due to increased stellar masses among the cluster galaxy population as being responsible for their lower f_{SF} (at all radii in Figure 2) with respect to the field. The progressive suppression in star formation in moving from field to infall regions, and on to cluster environments is seen at all stellar masses (compare dashed curves in Figure 3).

The *GALEX* NUV data provides a complementary means of identifying star-forming galaxies from their ultraviolet emission, and an opportunity to measure the SF-radius relation out to larger cluster-centric radii. Figure 4 shows the composite radial population gradient (magenta squares) in the fraction of cluster galaxies having blue rest-frame UV–optical colors $(NUV-r)_{0.0} < 4.5$, for the 23 clusters with deep *GALEX* NUV data and SDSS *ugriz* photometry. The $(NUV-r)_{0.0} = 4.5$ color limit lies in the middle of the UV–optical "green valley" (Wyder et al. 2007), and allows passively evolving galaxies to be efficiently excluded without losing dusty star-forming galaxies due to reddening (Haines et al. 2008). Optically quiescent early-type galaxies with residual (or "rejuvenated") extended star formation in the form of rings or spiral arms should also still be recovered (Salim & Rich 2010).

As before, the fraction of star-forming cluster galaxies increases steadily with cluster-centric radius from $f_{SF} \sim 0.11$ in the cluster core to $f_{SF} \sim 0.44$ at 4–$5r_{500}$ ($\sim 3r_{200}$). The fraction of star-forming cluster galaxies remains significantly below that seen in coeval field galaxies ($f_{SF} = 0.53 \pm 0.01$; magenta dashed line), even out at $\sim 5r_{500}$, the trend appearing to flatten off rather than continue upward to field values. Again the two samples are confirmed to be coeval: each radial bin for the cluster population has a mean redshift in the range 0.217–0.236, while for field galaxies $\langle z \rangle = 0.226$.

To allow comparison between the NUV-based and 24 μm-based SF–radius relations, the latter (gray points) is replotted from Figure 2 after adjusting its vertical scale (right-hand axis) to ensure that fractions of IR-selected and UV-selected star-forming field galaxies coincide on the plot. While both relations show the same steadily increasing trends with radius, the NUV-based SF-radius relation consistently lies above the re-scaled IR-based relation.

Looking at the IR-based SF-radius relation, it is tempting to suggest that the fraction of star-forming galaxies even falls to zero at the cluster core. However, we confirm that this is not the case. Further splitting each radial bin into four, the $f_{SF,IR}$ never fall below a floor value of $\sim 3\%$–5% in the cluster core. Similarly, the NUV-based SF-radius relation never falls below $\sim 8\%$–15% in the cluster core, when the radial bins are further sub-divided. A residual population of cluster galaxies with ongoing star formation exists at all radii.

3.2. Radial Surface Density Profiles

The spatial distribution of galaxies within clusters provides key constraints on the primary epoch at which they were

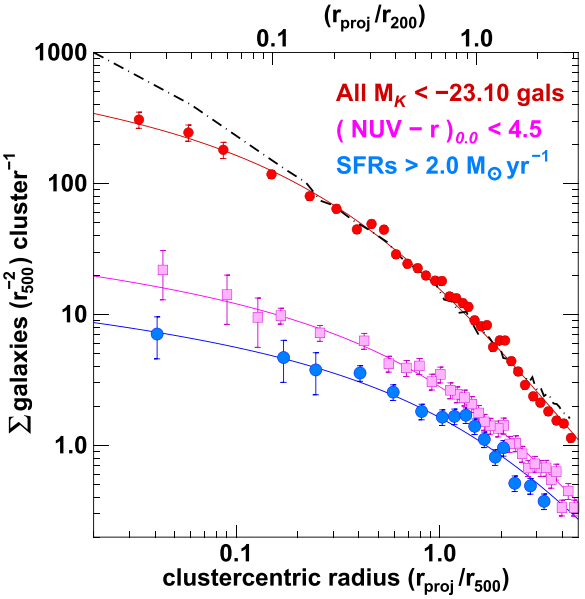

Figure 5. Composite galaxy surface density profile for *all* $M_K < M_K^* + 1.5$ galaxies (BCGs excluded) from our sample of $300.15 < z < 0.30$ clusters, as a function of projected cluster-centric radius ($r_{\rm proj}/r_{500}$). Each symbol consists of 200 spectroscopic cluster members. The blue symbols show the corresponding observed surface density $\Sigma(r)$ of $M_K < M_K^* + 1.5$ galaxies with active obscured star formation at rates $\rm SFR_{IR} > 2.0\,M_\odot\ yr^{-1}$ from the same ensemble cluster. The magenta squares show the radial profile for unobscured star-forming galaxies with $(\rm NUV - \it r)_{0.0} < 4.5$ from the 22 clusters that have SDSS *ugriz* and deep *GALEX* NUV photometry. The error bars assume Poisson statistics. The corresponding best-fit NFW profiles are shown by the red, blue and magenta curves. The dotted–dashed black curve shows the predicted surface density profiles for all "spectroscopic" member galaxies of the 75 most massive clusters from the Millennium simulation, scaled to fit our observed ensemble surface density profile of all galaxies.

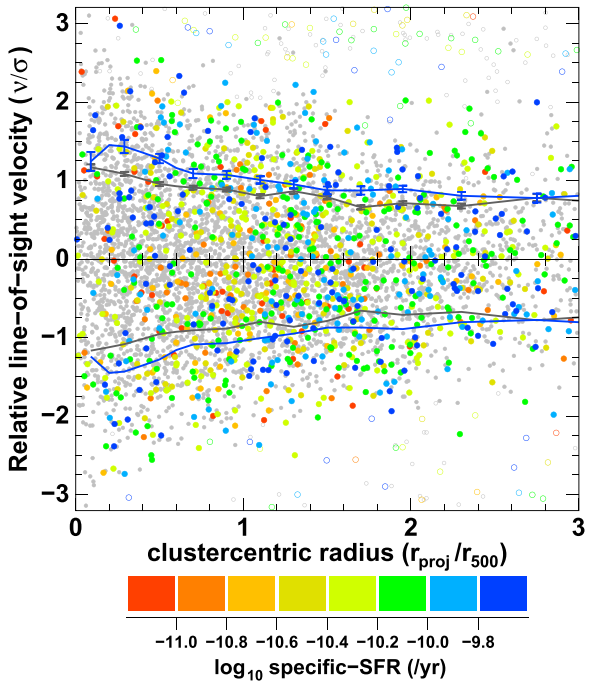

Figure 6. Stacked observed phase-space diagram, $(v_{\rm los} - \langle v \rangle)/\sigma_v$ vs. $r_{\rm proj}/r_{500}$, of galaxies combining all 30 clusters in our sample. Each gray solid dot represents a spectroscopic cluster member, while open points indicate non-cluster galaxies. Only those galaxies covered by our *Spitzer* data are plotted. Star-forming galaxies detected at 24 μm are indicated by larger symbols, colored according to their sSFRs from red ($\rm sSFR < 10^{-11}\ year^{-1}$) to blue ($\rm sSFR > 10^{-10}\ year^{-1}$). The blue curve and error bars indicate the 1-σ VDP of the 24 μm-detected cluster members. The uncertainty in each $\sigma(r)$ value is estimated by bootstrap resampling the galaxies in that radial bin. The black curve shows the corresponding radial profile for the remaining inactive cluster members.

accreted into the system, as well as the effects of continual cluster mass growth on their orbital parameters and tidal and ram-pressure stripping on their stellar masses. Figure 5 shows the radial distribution of all $M_K < M_K^* + 1.5$ galaxies in the stacked cluster out to $\sim 4 r_{500}$, excluding BCGs (red points).

Large numerical DM simulations have found that DM halos are well described by a "universal" two-parameter (NFW; Navarro et al. 1997) density profile from scales of 10 kpc out to 10 Mpc (Frenk et al 1999; Gao et al. 2012). The NFW profile is characterized by a scale radius $r_s = r_{200}/c$, where c is the concentration parameter. The three-dimensional density profile is given by $\rho(x) \propto x^{-1}(1+x)^{-2}$, where $x = r/r_s$, and $d \log \rho / d \log r = -2$ at $r = r_s$. The NFW model has been shown to provide excellent fits to stacked tangential shear profiles of massive clusters (Okabe et al. 2013), and the distribution of cluster galaxies (Lin et al. 2004). The surface density profile, $\Sigma(r)$, of cluster galaxies in our ensemble cluster sample can be well described by a projected NFW profile with a concentration parameter $c_g = 3.01 \pm 0.16$ (red curve), consistent with the $c_g = 2.90 \pm 0.22$ value obtained by Lin et al. (2004) or $c_g = 2.7 \pm 0.7$ obtained by Budzynski et al. (2012), while Muzzin et al. (2007) obtained a higher concentration of $c_g = 4.13 \pm 0.57$ for the stacked K-band number density profile of galaxies from 15 clusters at $0.2 < z < 0.55$. The c_g value of 3.01 obtained here is still significantly lower than the $c_{\rm WL,200} = 4.22^{+0.40}_{-0.36}$ value for the concentration of the overall mass distribution obtained by Okabe et al. (2013) from their weak lensing analysis of 50 $z \sim 0.2$ clusters, including many of the systems in our sample.

The surface density, $\Sigma(r)$, of massive $(M_K < M_K^* + 1.5)$ cluster galaxies with obscured $\rm SFR_{IR} > 2.0\,M_\odot\ yr^{-1}$ (blue points) declines steadily with radius from ~ 7 galaxies r_{500}^{-2} cluster^{-1} in the cluster cores to ~ 0.4 by $\sim 3 r_{500}$. These $\Sigma(r)$ include corrections for spectroscopic incompleteness (Section 2.4) and the radial variation in coverage by the 24 μm images (Section 2.2). Even though the *fraction* of star-forming galaxies is falling to close to zero in cluster cores, clusters mark over-densities in the spatial distribution of star-forming galaxies in the plane of the sky. This is simply due to the cuspy density profile of the global cluster galaxy population more than compensating for the steady decrease in $f_{\rm SF}$ when approaching the cluster core. The surface density of $M_K < M_K^* + 1.5$ cluster galaxies with $(\rm NUV - \it r)_{0.0} < 4.5$ (magenta squares) shows a similar radial profile, but is marginally steeper at small radii ($r_{\rm proj} \lesssim 0.2\,r_{500}$). We will show in Section 5.2 that these steadily declining trends in $\Sigma(r)$ imply that star formation must survive within recently accreted spirals for several Gyr to build up the apparent over-densities of star-forming cluster galaxies.

3.3. Dynamical Analysis of Star-forming Cluster Galaxies

Figure 6 shows the stacked caustic diagram of all 30 clusters, in which the projected radius of each cluster member is normalized by the *Chandra*-based r_{500} of that cluster, and the

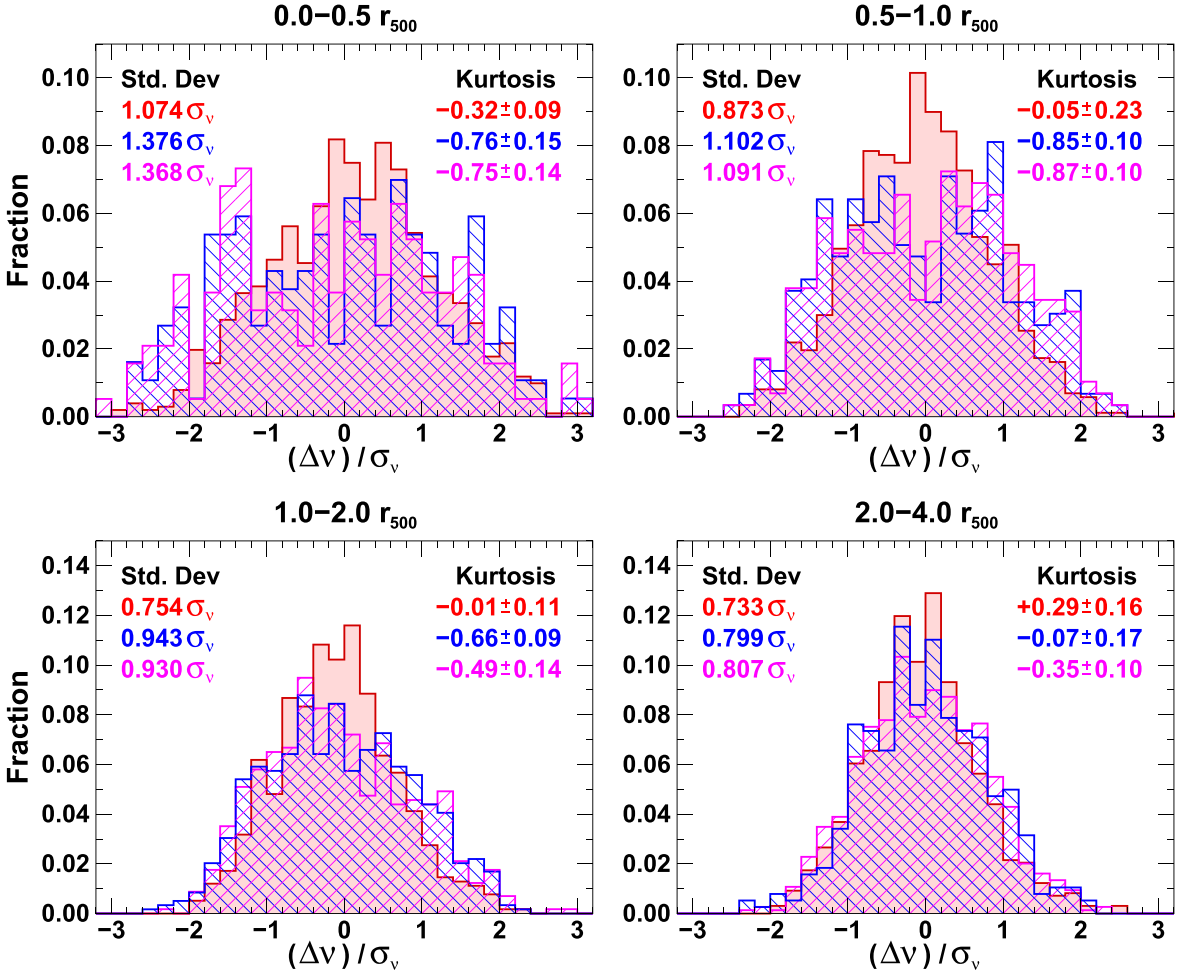

Figure 7. Stacked relative LOS velocity distributions of inactive galaxies (red solid histograms), 24 μm-detected (blue striped histogram), and UV-selected (NUV $-r < 4.5$; magenta striped histogram) star-forming galaxies from our ensemble cluster, in four bins of projected radius. The standard deviations (in units of σ_v) and kurtosis values of each distribution are indicated.

LOS velocities are scaled in units of σ_v. The 24 μm-detected star-forming galaxies (colored points) do not have the same spatial distribution within the caustic diagram as the remaining inactive cluster galaxy population (gray points). They appear to preferentially lie along the caustics, indicative of an infalling population. They also show a concentration at $r_{\rm proj} \sim 1.0$–$1.5r_{500}$, covering the full velocity range within the caustics. The fall off in numbers toward larger radii is a selection effect due to the decline in *Spitzer* 24 μm coverage beyond $2r_{500}$. Star-forming galaxies do not entirely avoid the central region with low cluster-centric radii ($r_{\rm proj} < 0.4\ r_{500}$) and relative LOS velocities ($|\Delta v/\sigma_v| \lesssim 0.80$), as X-ray AGNs appear to do (Haines et al. 2012), but their frequency certainly drops off here, in marked contrast to the inactive cluster galaxy population. Some of the star-forming galaxies in these central regions of phase-space will likely appear here due to projection effects, being located along the LOS of the cluster but physically still well outside r_{200} (see Figure 22).

The velocity dispersion of the star-forming cluster galaxy population (blue curve) is 10%–35% higher than that of the inactive cluster galaxies (gray curve) at all radii. Averaging over all galaxies within r_{500} ($2r_{500}$), star-forming galaxies have absolute LOS velocity offsets that are 26.4% (24.9%) higher than their passive counterparts at the same cluster-centric radius, a result significant at the 8.0σ (10.7σ) level.

The same trends are obtained when selecting star-forming cluster galaxies according to their rest-frame NUV$-r$ color. Their velocity dispersion remains 10%–35% higher than that of inactive cluster galaxies out to 2.5–$3r_{500}$, although at larger radii they become indistinguishable.

The relative LOS velocity distributions of star-forming (both 24 μm-detected and UV-selected) and inactive cluster galaxies for the stacked LoCuSS cluster sample are shown in Figure 7, in four bins of projected cluster-centric radius. The LOS velocity distributions of inactive galaxies (not detected at 24 μm and having $(\mathrm{NUV}-r)_{0.0} > 4.5$) can be approximately described as a Gaussian at all radii. The distributions of star-forming galaxies in the two inner radial bins ($r_{\rm proj} < r_{500}$) instead appear more consistent with a flat, top-hat profile than a Gaussian, including a relative excess of star-forming galaxies at $|\Delta v/\sigma_v| > 1.2$ in comparison to the inactive population. At 0.5–$1.0r_{500}$ there is even marginal evidence of a central dip in the LOS velocity distribution of star-forming galaxies. The kurtosis, $\gamma_2 = \left[\frac{1}{N}\sum_{i=1}^{N}(v_i-\bar{v})^4 \Big/ \left(\frac{1}{N},\sum_{i=1}^{N},(v_i-\bar{v})^2\right)^2\right] - 3$ of the LOS velocity distributions of star-forming galaxies ($\gamma_2 \sim -0.81$) is significantly lower than that expected for a Gaussian distribution ($\gamma_2 = 0.0$) at $>5\sigma$ level in both inner radial bins, and closer to expectations for a uniform top-hat distribution ($\gamma_2 = -1.2$). At large cluster-centric radii

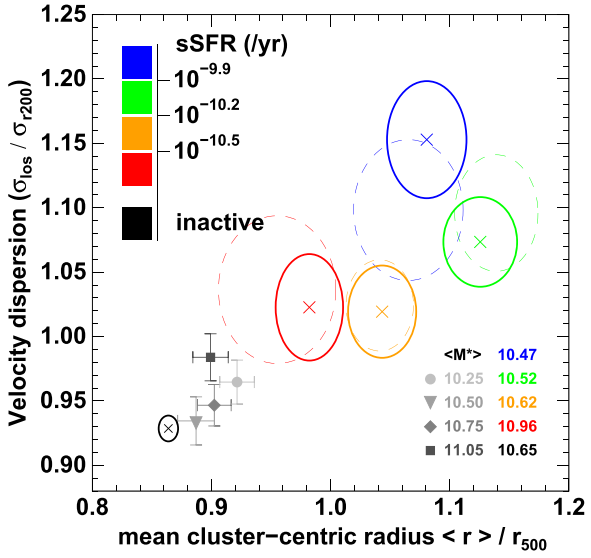

Figure 8. Variation in the spatial distribution and kinematics of cluster galaxies as a function of their sSFRs and stellar mass. Colored crosses indicate the mean cluster-centric radii ($\langle r_{\rm proj}/r_{500}\rangle$) and LOS velocity dispersions ($\sigma_{\rm los}(r_{\rm proj} < 2.0\ r_{500})/\sigma_v$) of star-forming cluster galaxies split into four bins of sSFRs. Error ellipses show the 1σ uncertainties in both values. The black cross indicates the corresponding values for inactive cluster galaxies not detected with *Spitzer* . Only cluster galaxies within $2r_{500}$ are included within each sub-sample. The mean stellar mass, $\langle\log(\mathcal{M}/M_\odot)\rangle$, of each sub-sample is indicated in the lower-right corner. Thin dashed ellipses indicate the results after applying additional stellar mass cuts to each sSFR bin to equalize their mean stellar masses to that of the inactive population. Grayscale symbols and error-bars indicate the mean cluster-centric radii and LOS velocity dispersions of cluster galaxies (including both star-forming and inactive sub-populations) split into four bins of stellar mass: $\log(\mathcal{M}/M_\odot) < 10.4$ (light gray circle); $10.4 < \log\mathcal{M} < 10.6$ (gray triangle); $10.6 < \log\mathcal{M} < 10.85$ (mid-gray diamond); $\log\mathcal{M} > 10.85$ (dark-gray square).

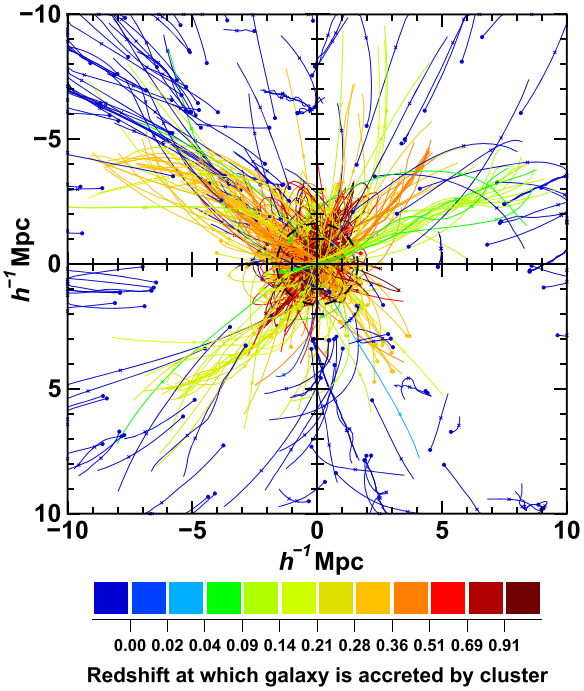

Figure 9. The orbits of galaxies about the 10th most massive cluster in the Millennium simulation, as viewed by a distant observer along the z-axis. The orbit of each galaxy with $\mathcal{M} > 2\times10^{10}\,M_\odot$ at $z = 0$ is shown by a colored curve, tracing its movement from $z = 0.76$ (snapshot 44) to $z = 0.0$ (snapshot 63). The final location of the galaxy is marked by a dot, while the cross indicates its location at $z = 0.41$ (snapshot 50). Each curve is color-coded according to the epoch at which the galaxy is accreted into the cluster, as indicated at the bottom of the plot. This accretion epoch is defined as the snapshot at which the galaxy passes within $r_{200}(z)$ for the first time. Galaxies yet to pass within r_{200} have mid-blue colors, while those accreted earliest into the cluster ($z_{\rm acc} > 0.51$) have red colors. The dashed black circle indicates the present day r_{200} radius of the cluster. Only galaxies which would be spectroscopically identified as cluster members by the observer are shown.

(2.0–4.0r_{500}), the velocity distribution of star-forming galaxies is consistent with a Gaussian function, and is almost indistinguishable from that of the inactive population, albeit with a marginally (∼9%) higher dispersion.

To further delineate the connection between the kinematics of cluster galaxies and their ability to form stars, the sample of 24 μm-detected cluster galaxies within $2.0r_{500}$ is split into four bins of sSFRs and their mean cluster-centric radii $\langle r_{\rm proj}/r_{500}\rangle$, and LOS velocity dispersions $\sigma_{\rm los}(<2\ r_{500})/\sigma_v$, compared in Figure 8. Kinematic segregation of galaxies with diverse sSFRs is apparent. Galaxies with the highest sSFRs ($\gtrsim10^{-9.9}$ year^{-1}; blue cross) have the highest velocity dispersion as a population, and a higher mean cluster-centric radius, than those star-forming galaxies with the lowest sSFRs ($<10^{-10.5}$ year^{-1}; red cross). There is a general progression toward lower mean radii and LOS velocity dispersions with decreasing sSFRs. This progression continues to the inactive galaxy cluster galaxy population (not detected at 24 μm; black cross), which has a significantly lower mean radius and velocity dispersion than any of the four sub-populations of star-forming galaxies.

The mean stellar masses of the star-forming cluster galaxies increases by 0.5 dex from the highest sSFR bin to those in the lowest one, reflecting the systematic decline in sSFRs with stellar mass for star-forming cluster galaxies (Haines et al. 2013). We may thus be concerned that these kinematical differences are in fact due to mass segregation rather than a sequence in declining sSFRs.

There is no evidence for mass segregation within our cluster galaxy population, however, consistent with von der Linden et al. (2010). Splitting the cluster galaxy population into bins of stellar mass (grayscale symbols), much less variation in the mean radii and LOS velocity dispersions is seen between stellar mass bins in comparison to those split by sSFRs, and no overall trend with stellar mass is visible. Moreover, the kinematic segregation by sSFRs persists even if additional stellar mass cuts are applied to each sSFR bin to equalize their mean stellar masses (thin dashed ellipses).

4. MAPPING THE CONTINUAL ACCRETION OF GALAXIES ONTO MASSIVE CLUSTERS IN THE MILLENNIUM SIMULATION

To correctly interpret the previous observed trends in cluster galaxy properties, clusters must be placed in the cosmological context of continually accreting galaxies and groups from their surroundings. With this aim, we have examined the spatial distributions and orbits of galaxies in the vicinity of the 75 most massive clusters from the Millennium simulation (Springel et al. 2005), a cosmological DM simulation covering a $(500h^{-1}{\rm Mpc})^3$ volume. These clusters have present day virial masses in the range $4.0–23.6\times10^{14}\,h^{-1}\,M_\odot$, velocity dispersions of 630–1540 km s^{-1}, and a median formation epoch, $z_f = 0.59$. We have extracted $20\times20\times140\,h^{-3}$ Mpc^3

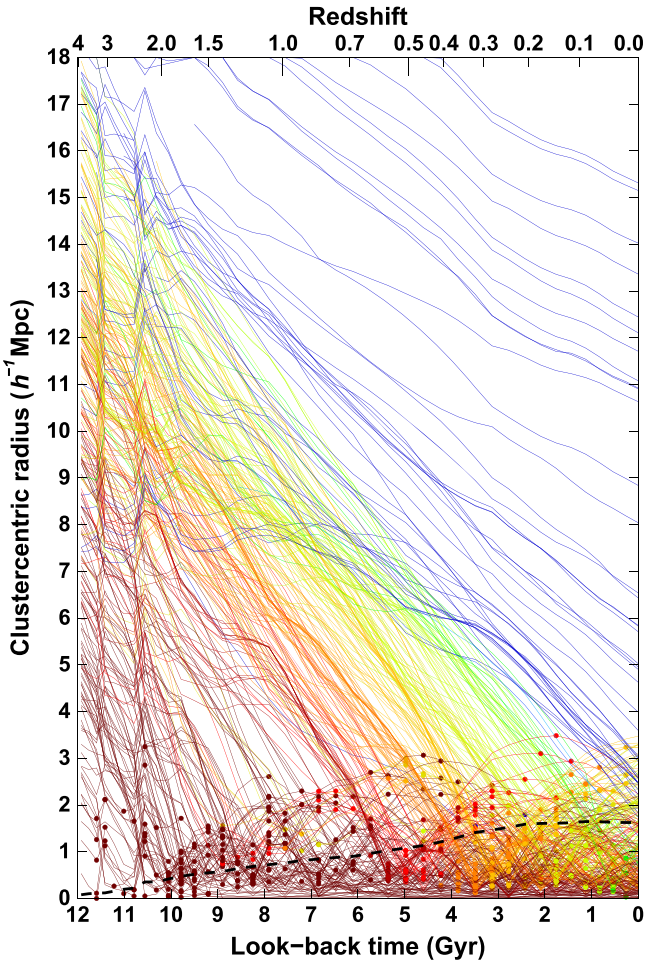

Figure 10. Infall of galaxies onto a massive cluster. Each galaxy with $\mathcal{M} > 2 \times 10^{10}\,M_{\odot}$ at $z = 0$ is shown by a colored curve tracing its comoving cluster-centric distance as a function of look-back time. The curves are color-coded according to the epoch at which the galaxy is accreted into the cluster, as in Figure 9. The first pericenter and apocenter of each galaxy's orbit about the cluster are marked with dots. The black dashed curve indicates the evolution of the cluster radius r_{200} with time. Only galaxies that would be spectroscopically identified as cluster members by the observer are shown.

volumes centered on each cluster. These volumes are extended in the z-direction so that, for a distant observer viewing along this axis, all galaxies with LOS velocities within 5000 km s^{-1} of the cluster redshift are included, enabling projection effects to be fully account for and quantified.

There exists a full database of properties for each galaxy in the simulation, including positions, peculiar velocities, absolute magnitudes, stellar masses, etc., based upon the GALFORM semi-analytic models (SAMs) of Bower et al. (2006) at 63 snapshots throughout the life-time of the universe to $z = 0$. Similarly, another database provides the positions, velocities, masses (M_{200}) and radii (r_{200}) of each DM halo at each snapshot. For each galaxy and halo in a given snapshot, the database provides links to identify its most massive progenitor in the preceding snapshot, and so on, all the way back to its formation, allowing its mass growth and full merger history to be mapped in detail (see e.g., De Lucia & Blaizot 2007). This process also allows the orbit of each galaxy with respect to the cluster to be followed from formation to the present day, enabling us to determine its epoch of accretion ($z_{\rm acc}$) into the cluster, defined here as the redshift at which the galaxy passes within $r_{200}(z)$ for the first time.

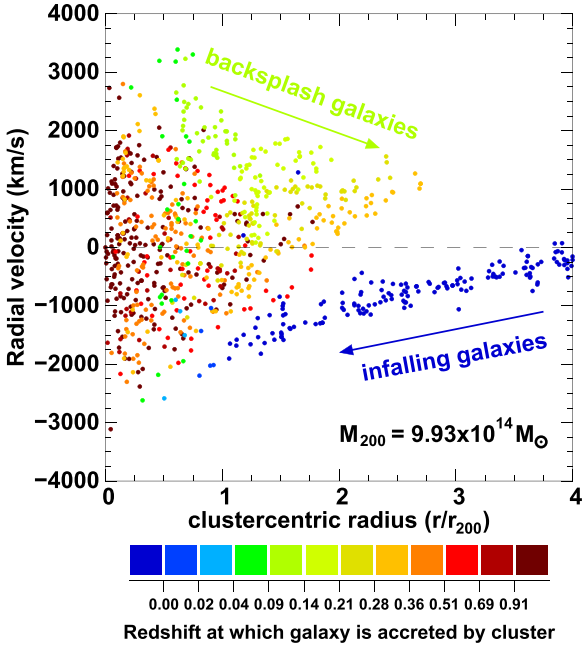

Figure 11. Radial phase-space diagram ($v_{\rm radial}$ vs. r/r_{200}) for galaxies with $\mathcal{M} > 5 \times 10^{9}\,M_{\odot}$ orbiting around the same massive cluster as in Figures 9 and 10. Galaxies are color-coded according to their accretion epoch as indicated.

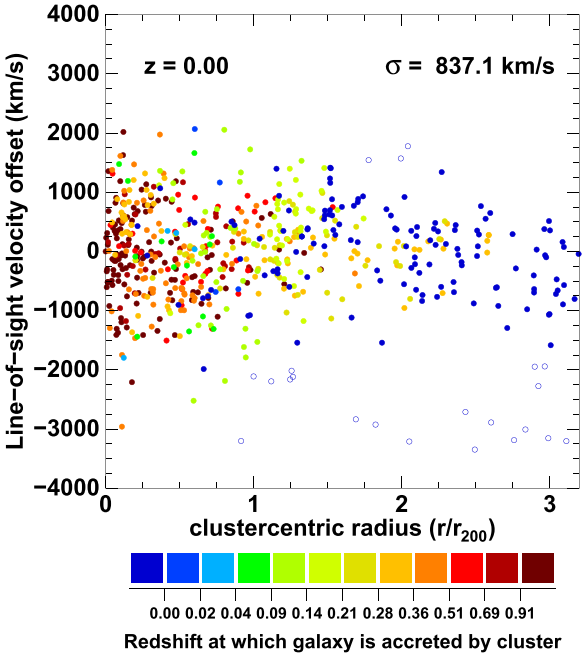

Figure 12. Caustic diagram ($\Delta v_{\rm los}$ vs. $r_{\rm proj}/r_{200}$) for $\mathcal{M} > 2 \times 10^{10}\,M_{\odot}$ galaxies orbiting around the same massive cluster, as viewed by distant observers along the z-axis. Galaxies are color-coded according to their accretion epoch as in Figures 9–11. Galaxies within $20h^{-1}$ Mpc of the cluster center at $z = 0.0$ are indicated by solid symbols, while those at comoving cluster-centric radii $r > 20h^{-1}$ Mpc are shown by open symbols. The velocity dispersion of galaxies within a projected cluster-centric radius $r_{\rm proj} < r_{200}$ is indicated.

4.1. The Infall of Galaxies onto Clusters

Figure 9 shows the orbits of galaxies about the tenth most massive cluster ($M_{200} = 9.9 \times 10^{14}\,h^{-1}\,M_{\odot}$ at $z = 0$) in the Millennium simulation, color-coded according to accretion epoch. Almost all the galaxies over the $20 \times 20\,h^{-2}$ Mpc^2 field

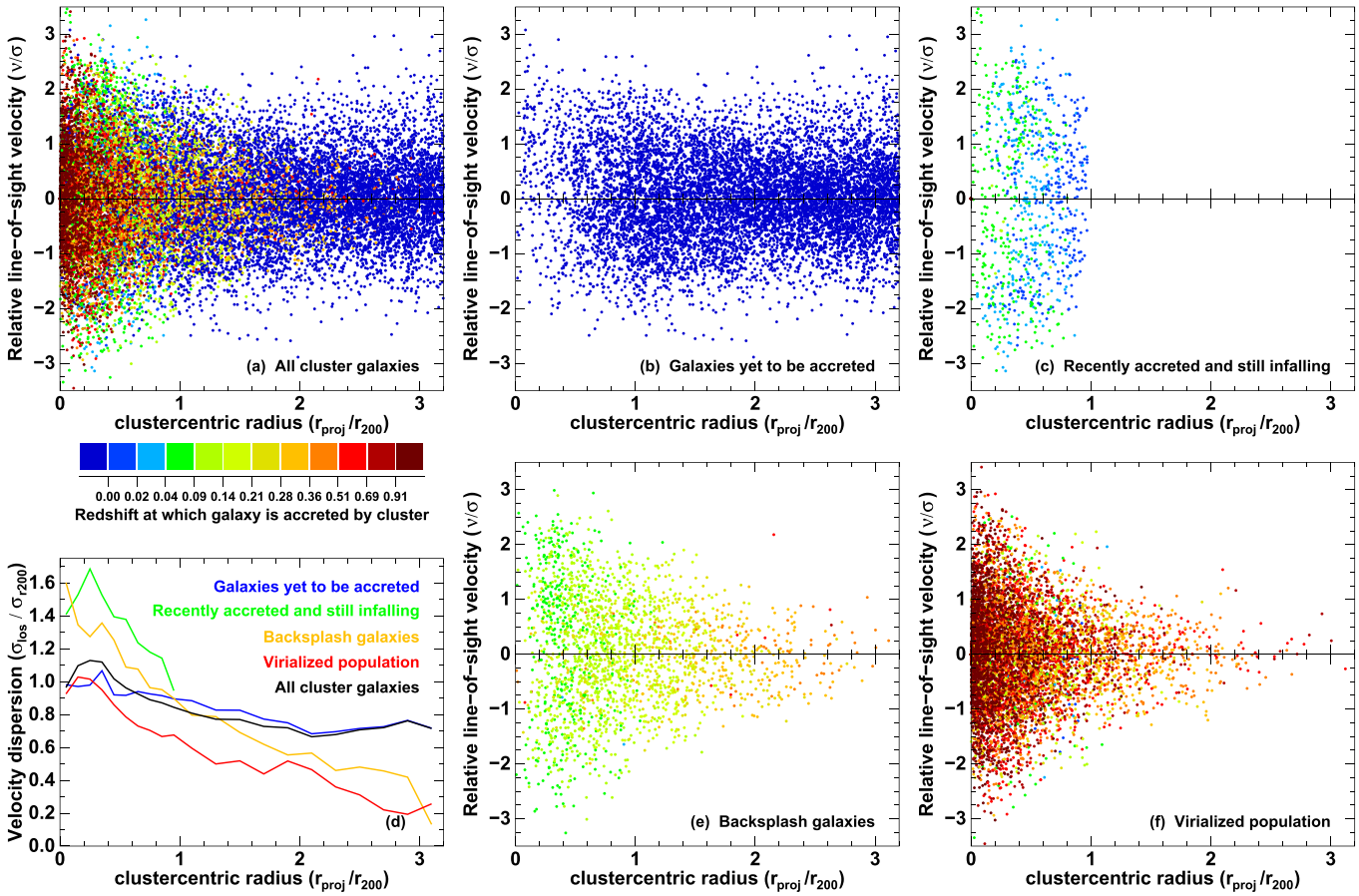

Figure 13. Stacked phase-space diagram ($\Delta v_{\rm los}/\sigma_v$ vs. $r_{\rm proj}/r_{200}$) for the 75 most massive clusters in the Millennium simulation at $z = 0.0$ (panel a). Each point indicates an $\mathcal{M} > 2 \times 10^{10}\,M_\odot$ galaxy from the Bower et al. (2006) semi-analytic model catalog, colored according to when it was accreted onto the cluster. The four panels on the right split these cluster galaxies into dynamical sub-populations: (b) just those galaxies yet to pass within r_{200} and be accreted into the cluster; (c) infalling galaxies ($v_{\rm radial} < 0$) which have passed within r_{200}, but have yet to reach pericenter; (e) back-splash galaxies which have passed through pericenter and are on their way back out of the cluster ($v_{\rm radial} > 0$) and are yet to reach apocenter; (f) the virialized cluster population which have passed through apocenter. The lower left panel (d) displays the velocity dispersion profiles ($\sigma_{\rm los}(r)/\sigma_v$) of each sub-population as well as that of the overall cluster population.

of view are falling steadily into the cluster or have already been accreted. The complex large-scale structure around the cluster is apparent, including clear preferential directions for the galaxies to flow into the cluster, while other regions appear largely devoid of galaxies. Galaxies tend to be drawn first into the filaments from the surrounding field, then flow along the filaments into the cluster. While many galaxies are infalling as individual objects from the field, others are arriving into the cluster within galaxy groups (e.g., the tangle of green curves coming in from the right-hand side).

The full extent of the cluster's gravitational sphere of influence is revealed in Figure 10, with all galaxies within 18 h^{-1} Mpc of the cluster falling steadily inward. For all 75 clusters, the boundary between the infall regions and beyond, where galaxies remain attached to the Hubble flow, is found at a comoving distance ∼10–20 h^{-1} Mpc from the cluster.

The infall of galaxies into the cluster is highly coherent, at least for $z \lesssim 1$: the radial velocities of infalling galaxies at the same cluster-centric radius at a given epoch are all roughly the same, and the future trajectories and accretion epochs of an infalling galaxy can be accurately estimated simply on the basis of their current cluster-centric distance. For example, almost all galaxies that were 5 h^{-1} Mpc from the cluster 4 billion years ago, are due to be accreted into the cluster at $z \sim 0.1$, as indicated by the parallel diagonal green colored curves.

After accretion, galaxies remain bound to the cluster, but many have orbits that take them outside r_{200} (*black dashed curve*), including some which bounce out as far as $\sim 2.5 r_{200}$. These galaxies, rebounding out of the cluster after their first pericenter passage are known as the "back-splash" population. The timescale required for galaxies to reach pericenter after being accreted is of the order 0.5–0.8 Gyr, while the orbital periods of the "back-splash" galaxies are much longer, only reaching their first apocenter 2–3 Gyr after passing through the cluster for the first time.

4.2. Phase-space Diagrams

Figure 11 shows the distribution of galaxies in radial phase-space: radial velocity ($v_{\rm radial}$) versus cluster-centric radius (r) in units of r_{200}, for the same cluster, where $v_{\rm radial}$ is the radial component of the galaxy's velocity relative to the cluster, including a component from the Hubble expansion ($H_0 r$).

The distribution of galaxies in phase-space splits into two reasonably well defined structures: a triangular-shaped virialized region containing galaxies which have passed through the cluster at least once; and a narrow stream of infalling galaxies (blue points) with negative radial velocities extending out to $4 r_{200}$ (Mamon et al. 2004; Dünner et al. 2007). As the infalling galaxies plunge into the deep gravitational potential well of the cluster, they are continually accelerated, reaching infall

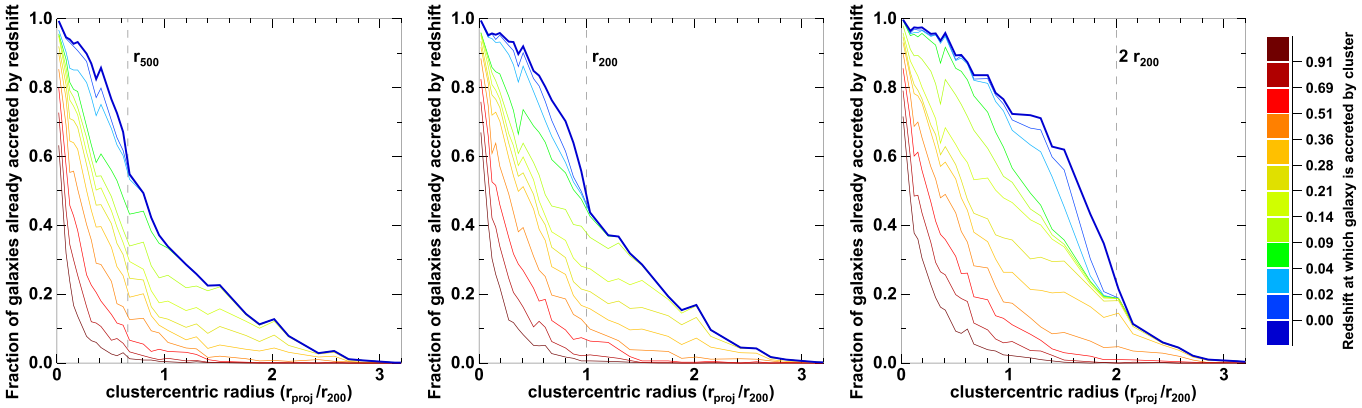

Figure 14. Radial population gradients in clusters. Each curve shows the fraction of "spectroscopic" cluster galaxies that have been accreted by a given redshift as a function of projected cluster-centric radius (normalized by r_{200}) averaged over our stacked sample of 75 massive clusters observed at $z = 0.0$, color-coded according to accretion redshift as indicated on the far right of the plot. The three panels indicate the trends produced when considering three definitions for describing when a galaxy is accreted into the cluster, taken to be the snapshot when the galaxy passes within r_{500} (left panel), r_{200} (middle panel), or $2r_{200}$ (right panel). The vertical dashed line in each panel indicates the corresponding radius at which the accretion epoch for the curves in that panel are defined.

velocities of up to 3000 km s^{-1}. After passing through pericenter, these galaxies reappear along the top edge of the triangular region as back-splash galaxies, coherently progressing outward and slowing down with increasing z_{acc} toward the right-hand apex at $\gtrsim 2r_{200}$ that marks the apocenter of the orbits of those galaxies accreted ~3 Gyr ago. The radial phase-space diagram retains much of the information regarding the epoch of accretion of a galaxy, allowing this epoch to be accurately estimated for galaxies based on their location in the diagram, at least for those accreted within the last 3 Gyr. Only those which were accreted much earlier have had time for their orbits to become mixed.

Figure 12 shows the observable counterpart to Figure 11: the caustic diagram, which plots the LOS velocity of galaxies relative to the cluster redshift (Δv_{los}) against projected cluster-centric radius (r_{proj}/r_{200}) for the same cluster, as viewed by a distant observer along the z-axis. The relative LOS velocity of galaxies combines the LOS component of their peculiar velocities with the contribution to their redshifts from the Hubble expansion: $\Delta v_{los} = (v_{z,gal} - v_{z,cl}) + H_0\, d_z$, where $v_{z,gal}$ and $v_{z,cl}$ are the LOS peculiar velocities of the galaxy and cluster DM halo respectively, and d_z is the distance between the galaxy and the cluster halo along the LOS.

The distribution of cluster galaxies shows the typical "trumpet"-shaped caustic profile. Throughout this paper we refer to "spectroscopic" cluster members as those galaxies which lie within the caustic profiles determined for each of the 75 clusters. This is not the same as galaxies which are identified as satellites of the cluster DM halo, which are those physically located within the cluster halo ($r < r_{200}$), or even the population of accreted galaxies that have passed within $r_{200}(z)$ at some point in their history (but which may now be outside r_{200}). For this cluster, the separation between those galaxies that would be identified as "spectroscopic" cluster members, and those which are clearly background objects, roughly corresponds to a separation between those physically within $20h^{-1}$ Mpc of the cluster center (solid points), and those beyond this radius (open points). Indeed, all the galaxies shown earlier in Figure 10 are "spectroscopic" cluster members within a projected cluster-centric radius $2.0r_{200}$. Examining each of the 75 clusters individually, the cluster-centric distances that best separate "spectroscopic" members and clear fore/background objects are $19 \pm 3\ h^{-1}$ Mpc $(13 \pm 2r_{200})$.

Unlike the radial phase-space diagram, it is not possible to select individual galaxies from a specific region of the caustic diagram and then identify it as an infalling, recently accreted or virialized galaxy. However, several trends within the distribution of galaxies in the caustic diagram can be seen. First, those galaxies accreted earliest ($z_{acc} \gtrsim 0.4$; red points) are spatially localized in the cluster core with typical LOS velocities $\lesssim$1 000 km s^{-1}. Second, beyond $r_{proj} \gtrsim 1.8\ r_{200}$ the bulk of galaxies have yet to be accreted into the cluster while the remainder all appear to be back-splash galaxies accreted ~3 Gyr ago. Finally, many of the galaxies with the largest LOS velocities ($\gtrsim$1000 km s^{-1}) have only recently arrived into the cluster (green points). Although these general trends hold for the vast majority of the clusters in our sample, there is significant cluster-to-cluster variation in the spatial distributions and relative contributions of galaxies accreted at different epochs, as expected given their dynamical immaturity.

4.3. Stacking the Clusters

To account for the cluster-to-cluster scatter in a statistical way, the caustic diagrams for all 75 clusters are stacked to produce Figure 13(a). The cluster-centric radius of each cluster member is scaled by the r_{200} of that cluster, and the LOS velocities are scaled in units of $\sigma_v(r_{proj} < r_{200})$, the LOS velocity dispersion of all "spectroscopic" members within r_{200}.

To demonstrate how the distribution of galaxy populations in the caustic plot provides information about their dynamical evolution and accretion history, the right-hand panels show the caustic diagrams after splitting the cluster population into four dynamical sub-populations, while panel (d) plots each of their velocity dispersion profiles (VDPs) $\sigma_{los}(r)/\sigma_v$ alongside that for the overall cluster population. First, galaxies yet to pass within r_{200} and be accreted (panel b) are found at all cluster-centric radii, becoming increasingly dominant with radius. The fall in numbers toward the cluster core ($r_{proj} \lesssim 0.6\ r_{200}$) is due to the area of sky covered in any given narrow radial slice scaling as r, rather than a physical decline in the surface density of such galaxies at low radii (see Figure 17). The velocity dispersion of these galaxies remains relatively constant with radius, as they have yet to approach the cluster core.

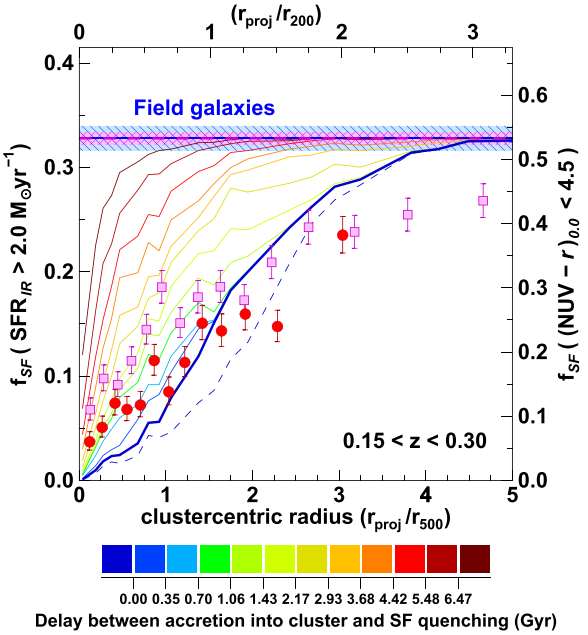

Figure 15. Comparison of the observed radial population gradients with predictions from cosmological simulations. The red points show the fractions of $\mathcal{M} > 2 \times 10^{10}\,M_{\odot}$ cluster galaxies with obscured SFR $> 2.0\,M_{\odot}$ yr^{-1} from Figure 2, while the magenta squares show the corresponding SF-radius relation for UV-selected star-forming galaxies (Figure 4). The blue horizontal line indicates the corresponding fraction of field galaxies ($\mathcal{M} > 2 \times 10^{10}\,M_{\odot}$; $0.15 < z < 0.30$) with SFR$_{\rm IR} > 2.0\,M_{\odot}$ yr^{-1}, while the blue shaded region indicates the 1σ confidence levels. The thick blue diagonal curve shows the predicted SF-radius relation obtained from our "observations" of the 75 massive clusters in the Millennium simulation, assuming that infalling galaxies have the same $f_{\rm SF}$ as our observed field galaxy sample, and star formation is immediately quenched upon being accreted into the cluster, i.e., passing within r_{200} for the first time. The colored curves show the effects of delaying this quenching by a time Δt after the galaxy is accreted into the cluster, as indicated by the color scale below the plot. The dashed blue curve shows the effect on the predicted SF-radius relation of changing the cluster-centric radius at which quenching is initiated from r_{200} out to $2r_{200}$.

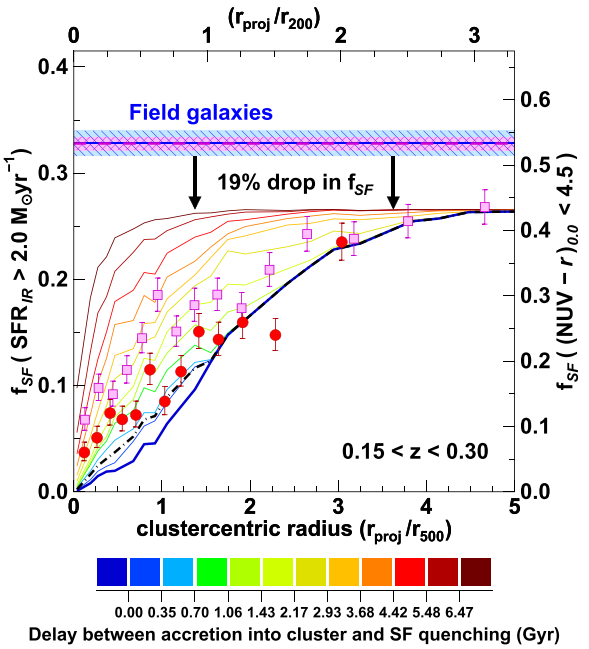

Figure 16. Radial population gradients. The red and magenta points show the observed IR- and UV-based SF-radius relations as in Figure 15. The colored curves are the same as those in Figure 15, except that they now assume that the infalling galaxies have a fraction $f_{\rm SF}$ which has been reduced by 19% with respect to that seen in the general field (blue horizontal line). The black dotted–dashed curve indicates the predicted SF-radius relation in the case that star formation is instantaneously quenched when galaxies reach pericenter.

Panel (c) shows those infalling galaxies which have recently passed within r_{200} for the first time, but have yet to reach pericenter. These objects are all found within r_{200} by default. They have the highest LOS velocities of all our sub-populations ($\sigma_{\rm los}(r) \gtrsim 1.4\,\sigma_{\nu}$), being fully accelerated as they fall deep into the gravitational potential well of the cluster core, and at late epochs when the clusters are much more massive than at any previous point in their history.

Panel (e) shows the back-splash population of cluster galaxies that have passed through pericenter, and are now heading back out away from the cluster center ($\nu_{\rm radial} > 0$), but have yet to reach apocenter. These galaxies were typically accreted 1–4 Gyr ago. This population shows a triangular distribution in the caustic diagram, with high LOS-velocities ($\sigma_{\rm los} \sim 1.3$–$1.5\,\sigma_{\nu}$) in the cluster core, having recently completed their first infall, which steadily fall as the galaxies rebound out of the cluster, slowing down as they attempt to climb back out of its potential well. The back-splash population extends as far out as 2–$3r_{200}$, where they can be differentiated from the infalling population by their characteristically low LOS-velocity dispersions ($\sigma_{\rm los}(r) \sim 0.4$–$0.55\,\sigma_{\nu}$), some ~35% lower than the overall cluster population at the same cluster-centric distances (see Gill et al. 2005).

Finally, the virialized population (panel f) are those galaxies which were accreted at early epochs ($z_{\rm acc} \gtrsim 0.4$) and have all passed through apocenter of their first orbit. This population also presents a triangular distribution in the caustic diagram, but is much more concentrated toward the cluster core (particularly at $\lesssim 0.2r_{200}$) than the back-splash galaxies, and has lower LOS-velocity dispersions at all radii. We identify this population with those galaxies that either formed locally or were accreted when the cluster's core was being assembled. Their low velocities reflect the fact that the system they fell into was much less massive than the present-day cluster.

4.4. Radial Population Gradients

Figure 14 shows the radial population gradients obtained when stacking the 75 massive clusters as observed at $z = 0.0$. The thick blue curve in the middle panel shows how the fraction of "spectroscopic" cluster members that have been accreted varies as a function of projected cluster-centric radius, $r_{\rm proj}/r_{200}$. This fraction drops slowly from 100% at the cluster core to ~90% at $0.4r_{200}$, before falling at an ever-increasing rate down to ~50% by r_{200}, and approaching zero by $\sim 3r_{200}$. For $r_{\rm proj} > r_{200}$, this contribution represents the "back-splash" population galaxies that have previously been accreted into the cluster, but now have bounced back out beyond r_{200}.

The remaining curves show the effects on this fraction by progressively excluding galaxies that were accreted after a given redshift. The first three curves ($z_{\rm acc} < 0.09$) only diverge from the top curve at $r_{\rm proj} < r_{200}$, as the most recently accreted galaxies haven't had sufficient time to pass though the cluster and go back out beyond r_{200}. As those galaxies accreted 1–3 Gyr ago are progressively excluded, the curves become increasingly steep within r_{200}, and flatter beyond r_{200}. The bulk

of the "back-splash" population found beyond r_{200} was accreted between $z = 0.14$ and $z = 0.51$.

The remaining panels show the effect of changing the nominal radius for identifying when a galaxy has been accreted into a cluster. Reducing the accretion radius from r_{200} to r_{500} (left panel) simply squeezes the curves inward by a comparable amount. Pushing the accretion radius outward to $2r_{200}$ (right panel) increases the prominence of the bump produced by recently accreted galaxies, but greatly reduces the contribution from back-splash galaxies, as so few galaxies which pass within $2r_{200}$ rebound from the cluster beyond this radius.

The key aspect of all these curves is that irrespective of accretion epoch, z_{acc}, or the precise radius used to define accretion (within reasonable limits), the resulting radial population gradient drops from ∼100% in the cluster core to zero by $\sim 3r_{200}$. This steep gradient is primarily due to the complementary increase with radius in the fraction of "interloper" galaxies that have yet to be accreted into the cluster among the "spectroscopic" cluster population, from zero in the cluster core to 100% by $\sim 3r_{200}$. A second contribution to the steepness comes from the correlations between the epoch of accretion of *satellite* galaxies and their present cluster-centric distance (De Lucia et al. 2012), with those satellite galaxies close to the cluster core having been accreted significantly earlier on average than those located close to the virial radius (both physically or in projection). Gao et al. (2004) find the same radial trend for sub-halos, with the median accretion redshift of sub-halos in massive cluster halos decreasing from $z_{acc} \sim 1.0$ in the cluster core to $z_{acc} \sim 0.4$ at r_{200} (their Figure 15).

5. CONSTRAINING STAR FORMATION QUENCHING MODELS BY COMPARISON TO THE OBSERVED SF-RADIUS TRENDS

Figures 2–4 showed that the fraction of massive cluster galaxies with $SFR_{IR} > 2.0\ M_\odot\ yr^{-1}$ or blue UV–optical colors increases steadily with cluster-centric radius, but at the largest radii probed, the f_{SF} remained significantly (20%–30%) below that seen in coeval field galaxies in both cases.

In Figure 15 we attempt to reproduce these two SF-radius trends using a simple toy model in which the star formation of infalling field galaxies is instantaneously quenched at the moment they pass within r_{200} of the cluster for the first time, or after a certain time delay (Δt). The fraction of star-forming galaxies among this infalling field population is set to match our observed coeval field galaxy sample. The stacked radial population gradients for $\mathcal{M} > 2 \times 10^{10}\ M_\odot$ galaxies from the same 75 massive clusters in the Millennium simulation are reproduced, as they would appear if observed at $z = 0.21$, to best match the redshifts of the LoCuSS sample. The model galaxy positions and velocities relative to the cluster halo are now measured as they stood at $z = 0.21$, while the clusters are stacked using their r_{200} and σ_ν values measured at $z = 0.21$. At $z = 0.21$ these clusters have M_{200} masses in the range 2.6–21. $7 \times 10^{14}\ h^{-1}\ M_\odot$, with a median M_{200} of $5.0 \times 10^{14}\ h^{-1}\ M_\odot$.

The predicted SF-radius relation in the case that star formation in all infalling galaxies is instantaneously quenched upon accretion (thick blue diagonal curve) is qualitatively similar in form to the observed trends, and consistent with the data points at ~ 1–$2r_{500}$, suggesting that this is to first order a reasonable assumption, as found previously by Balogh et al. (2000) and Haines et al. (2009). The model radial gradient is too steep, however, resulting in predicted values of f_{SF} that are much higher than our data points in the range 1.8–$3.0r_{500}$, and too low in the cluster core ($r_{proj} \lesssim 0.8r_{500}$).

The remaining colored curves show the effects of delaying the moment at which quenching occurs, by terminating star formation only in those galaxies accreted into the cluster more than Δt Gyr prior to observation, corresponding to the "delayed-then-rapid" quenching scenario of Wetzel et al. (2013). The "excess" obscured star formation (red points) observed in the cluster core can then be reasonably reproduced by a model with a short quenching delay of the order 0.3–1.0 Gyr (light-blue/green curves). Much longer quenching time-delays ($\Delta t \gtrsim 3$ Gyr) are clearly excluded, as they leave too many star-forming galaxies at $r_{proj} \sim 1$–$2r_{500}$.

One possible way to reconcile the model predictions with our data at ~ 3–$5r_{500}$ would be to initiate the quenching process at larger radii. The dashed curve shows the radial population gradient produced when star formation in all infalling galaxies is immediately quenched when they pass within $2r_{200}$ for the first time (rather than r_{200} as before). While the fraction of star-forming galaxies has now been reduced sufficiently at $\sim 2r_{500}$, the gradient of the model trend remains much steeper than that observed, and vastly under-predicts the fraction of star-forming galaxies at $r_{proj} \lesssim 1.5\ r_{500}$.

The model curves provide little or no leeway to reproduce the low f_{SF} observed over 3–$5r_{500}$ in the NUV-based SF-radius relation (magenta squares), as they all approach the field value at 3.5–$4.0r_{500}$ (∼2.5–$3.0r_{200}$), the radius at which the fraction of back-splash galaxies falls to zero (Figure 14), irrespective of the radius at which quenching is initiated.

The only way to improve the model fits to these observations would be to allow the fraction of star-forming galaxies among the infalling population to be *lower* than that observed among the general coeval field population. We consider the simplest approach in Figure 16, that of simply reducing the f_{SF} of cluster galaxies by a single fixed amount (19%) from the value observed in the field, at all radii, to model the impact of whatever physical process is reducing star formation among galaxies in the infall regions of clusters. One feasible mechanism to achieve this is via the "pre-processing" of galaxies within galaxy groups which are subsequently accreted into clusters. The cosmological simulations of Gabor & Davé (2015) suggest that ∼40% of satellite galaxies within clusters are pre-processed, the fraction decreasing weakly with cluster-centric radius. The overall IR-based SF-radius relation can now be reproduced at all radii, via a model in which star formation is quenched in galaxies ∼0.7–1.5 Gyr after being accreted into the cluster. This occurs on average *after* the galaxy has passed through the cluster core, as the observed trend lies above that predicted for the case in which star formation is quenched in galaxies at the moment they reach pericenter (black dotted–dashed curve).

The NUV-based SF-radius relation is systematically above that of the IR-based inside $\sim 2.5r_{500}$, and is best-fit by a model in which star formation is quenched in galaxies ∼2.1–3.6 Gyr after accretion, or slightly later than that suggested by the IR-based relation.

For all these model curves, to use the terminology of Peng et al. (2010, 2012), we assume that the environmental quenching process is 100% efficient ($\epsilon_{sat} = 1$), i.e., *all* star-forming galaxies are quenched Δt Gyr after accretion into the cluster. The result of decreasing ϵ_{sat} for clusters would leave the model

curves unchanged at large radii ($r_{\rm proj} \gtrsim 3r_{200}$), but squeeze the curves upward in the core, effectively reducing the radial population *gradient* by a factor $(1 - \epsilon_{\rm sat})$. The fact that the observed gradients are steep, with $f_{\rm SF}$ increasing fivefold over 0–$3r_{200}$, necessitates a high environmental quenching efficiency, $\epsilon_{\rm sat} \gtrsim 0.8$, otherwise there would be evidence of a residual population of primordial cluster galaxies with ongoing star formation in cluster cores ($r_{\rm proj} \lesssim 0.1r_{200}$).

5.1. Uncertainties in the Model Trends

One concern about attempting to fit the SF-radius relation with model curves is that the latter require the SAMs to reliably follow the orbits of cluster galaxies long after their accretion and accurately model the long-term evolution of their stellar masses once they become satellites. The Millennium simulation itself considers only the DM component, the baryons bolted on afterward via SAMs.

When galaxies are accreted into massive clusters, their parent DM halos become sub-halos of the cluster halo, losing mass continuously through tidal stripping, until in many cases they fall below the resolution limit of the simulation, dissolving into the parent halo or are completely disrupted (Gao et al. 2004; Weinmann et al. 2010). The galaxies hosted by these sub-halos are much more compact and tightly bound than the DM, and as long as some of the surrounding sub-halo survives, are not expected to suffer significant stellar mass loss, although their diffuse hot gas halo is likely to be lost at a rate commensurate with that of the parent sub-halo (Guo et al. 2011). Prior to their accretion into the clusters, model galaxies at our lower stellar mass limit of $2 \times 10^{10}\,M_{\odot}$ typically have parent DM halos of masses $\sim 6 \times 10^{11}\,h^{-1}\,M_{\odot}$ in the Millennium simulation, comprising ~730 DM particles, and hence must suffer >95% stripping before their parent sub-halo falls below the mass resolution limit of 20 particles (Springel et al. 2005), a process which typically takes ~5 Gyr (Weinmann et al. 2010). Even after their parent sub-halo has been entirely disrupted, they are expected to survive as "orphan" galaxies, although now they will be likely subject to significant stellar mass loss via tidal stripping and may be completely disrupted.

The inclusion and treatment of "orphan" galaxies by SAMs is required to explain the cuspy radial satellite number density profiles observed within cluster halos (Figure 17), which are much steeper than the relatively flat radial distributions of DM sub-halos within $0.3r_{500}$ (Budzynski et al. 2012; Vogelsberger et al. 2014). These SAMs resort to ad hoc prescriptions for mass-stripping and adjustment of the orbits of these "orphan" galaxies within the cluster halos, resulting in strong variations in the radial satellite number density profiles within cluster cores (Budzynski et al. 2012), and the fractions of "orphans" in the cluster satellite population, from 25% in the Guo et al. (2011) model to 50% in the Bower et al. (2006) model (Gifford et al. 2013). This likely explains the inability of the predicted radial profile of model cluster galaxies from the Bower et al. (2006) SAM to match the observed radial profile at $r_{\rm proj} \lesssim 0.1\ r_{500}$, overestimating the number density of cluster galaxies by a factor 2–3 (Figure 5).

We should therefore be cautious about using model curves, such as those in Figures 15 and 16, that depend upon the radial distribution and numbers of those galaxies accreted earliest into the clusters, and which have suffered repeated interactions over multiple orbits within the ever growing cluster halo. All the model curves in these two figures do this, even those referring to galaxies yet to be accreted into cluster, as they depend upon the relative contributions of those accreted after a given epoch, with all those accreted before the same epoch.

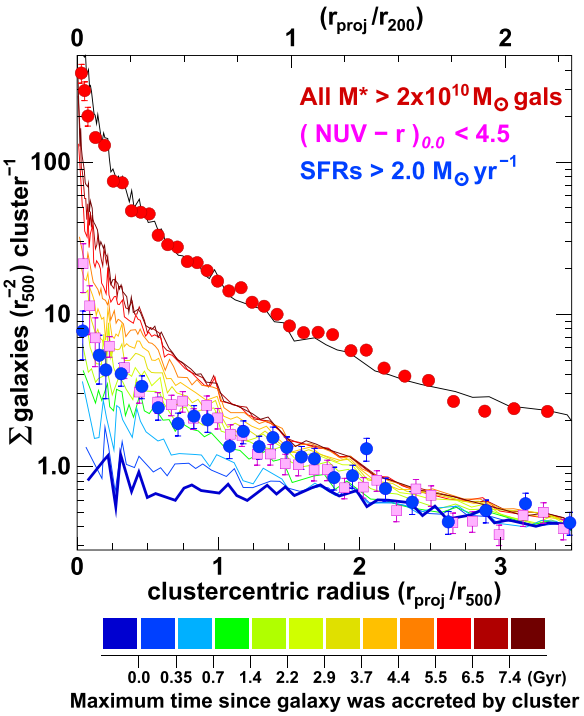

Figure 17. Blue symbols show the $\Sigma(r)$ profile of $\mathcal{M} > 2 \times 10^{10}\,M_{\odot}$ galaxies with obscured star formation at rates ${\rm SFR_{IR}} > 2.0\,M_{\odot}\ {\rm yr}^{-1}$ averaged over our 30 clusters. Magenta squares show the $\Sigma(r)$ profile for unobscured star-forming galaxies with $({\rm NUV} - r)_{0.0} < 4.5$, normalized to match the profile of obscured star-forming galaxies at $r_{\rm proj} \gtrsim 1.5\,r_{500}$. The thick blue curve shows the predicted surface density profile of infalling galaxies yet to pass within r_{200}, obtained from our "observations" of the 75 massive clusters in the Millennium simulation at $z = 0.21$, normalized to fit the observed radial profiles of star-forming galaxies at large radii. The remaining colored curves show the predicted radial profiles produced by including also those galaxies accreted into the clusters within the last Δt Gyr as indicated by the color scale. The black curve shows the predicted surface density profile for all "spectroscopic" member galaxies of the same 75 clusters, scaled to best match the observed ensemble $\Sigma(r)$ profile of *all* $\mathcal{M} > 2 \times 10^{10}\,M_{\odot}$ cluster galaxies (red points).

5.2. Radial Galaxy Surface Density Profiles

Figure 17 compares the radial galaxy surface density profiles, $\Sigma(r)$, of star-forming galaxies with model surface density profiles considering just those galaxies accreted within the last Δt Gyr or which have not yet been accreted. This plot largely resolves the above issues, by focusing solely on star-forming galaxies, which are most likely to still have surviving parent sub-halos, and comparison model curves that contain just the most recent arrivals into clusters, and hence minimizing the uncertain contribution from "orphan" galaxies.

The surface density of star-forming $({\rm SFR_{IR}} > 2.0\,M_{\odot}\ {\rm yr}^{-1})$ cluster galaxies from our ensemble of 30 clusters (blue points) declines steadily with radius out to $\sim 3r_{500}$, with no evidence of flattening off inside r_{500}. This immediately rules out models in which star formation is instantaneously quenched when galaxies are accreted into clusters (thick blue curve), as these produce radial profiles which are essentially flat within $2r_{500}$. As recently accreted galaxies are progressively included, the radial density profile steadily builds up and steepens within

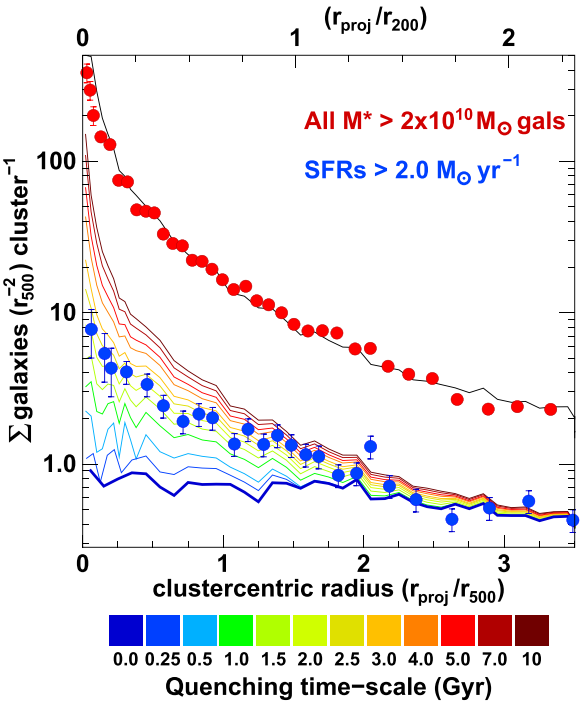

Figure 18. Blue symbols show the $\Sigma(r)$ profile of $\mathcal{M} > 2 \times 10^{10} M_{\odot}$ galaxies with obscured star formation at rates $\mathrm{SFR_{IR}} > 2.0\,M_{\odot}\ \mathrm{yr}^{-1}$. Red symbols indicate the corresponding $\Sigma(r)$ profile for *all* $\mathcal{M} > 2 \times 10^{10} M_{\odot}$ galaxies. The thick blue curve shows the predicted surface density profile of infalling galaxies yet to pass within r_{200}, normalized to fit the observed surface density profile of star-forming galaxies at large radii. The remaining colored curves show the predicted surface density profiles for star-forming galaxies accreted into the clusters and subsequently have their star formation rates decline exponentially with a range of quenching timescales ($t_Q = 0$ .25–10 Gyr).

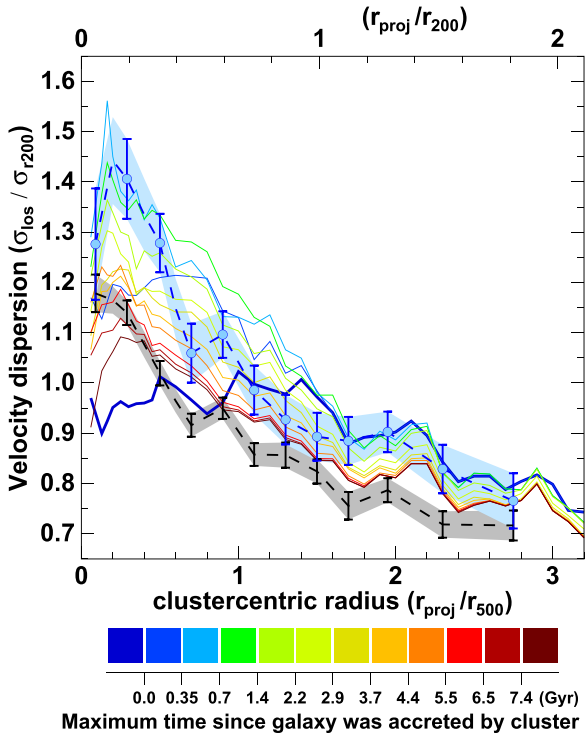

Figure 19. Predicted velocity dispersion profiles as a function of accretion epoch for model galaxies in our stacked sample of 75 clusters from the Millennium simulation at $z = 0.21$. The thick blue curve shows the predicted LOS velocity dispersion profile of "spectroscopic" cluster members yet to pass within r_{200} and be accreted into the cluster DM halo. The remaining solid curves show the impact on the velocity dispersion of progressively including those galaxies accreted into the clusters within the last Δt Gyr as indicated by the color scale. The black solid curve shows the velocity dispersion profile obtained by including all cluster members. Blue symbols with error bars show the *observed* velocity dispersion profile of the 24 μm-detected cluster members from our stacked sample of 30 clusters. The black dashed curve shows the corresponding profile considering all $\mathcal{M} > 2 \times 10^{10}\,M_{\odot}$ cluster members.

$2r_{500}$. The best-fitting curve to the *Spitzer* data is obtained by considering those model cluster galaxies accreted within the last $\Delta t = 2.1^{+0.8}_{-0.7}$ Gyr, with a χ^2 value of 21.15 for 23 data points and two degrees of freedom (ϕ and Δt). The uncertainties in Δt are derived as the values for which the χ^2 value has increased by 2.30 from the minimum value.

Outside of $0.3r_{500}$, the shape of the $\Sigma(r)$ profile for unobscured star-forming galaxies (magenta squares; $\mathcal{M} > 2 \times 10^{10}\,M_{\odot}$, $(\mathrm{NUV}-r)_{0.0} < 4.5$), coincides well with that of the obscured star-forming population. In contrast, the $\Sigma(r)$ profile for the UV-selected star-forming galaxies steepens more rapidly in the cluster core to form a cusp, paralleling that seen for the overall cluster population (red points). The best-fitting curve to the NUV data has $\Delta t = 3.2 \pm 0.4$ Gyr ($\chi^2 = 29.57$ for 32 data points), implying that the NUV emission takes 1.1 Gyr longer after accretion to be shut down than the 24 μm emission.

Figure 18 replots the $\Sigma(r)$ profile for obscured star-forming cluster galaxies (blue points), but now compares it with slow quenching models. In this scenario model star-forming galaxies are accreted into the cluster and subsequently gradually quenched, their SFRs declining exponentially on a quenching timescale t_Q until their SFRs fall below our nominal limit of $2.0 M_{\odot}\ \mathrm{yr}^{-1}$. These model star-forming galaxies are given initial SFRs taken at random from our observed sample of coeval *field* star-forming galaxies ($\mathrm{SFR} > 2\,M_{\odot}\ \mathrm{yr}^{-1}$; $0.15 < z < 0.30$), the SFR distribution of which is shown in Figure 2 of Haines et al. (2013). This should be reasonable given that the infrared luminosity functions of cluster and field galaxies are indistinguishable (Finn et al. 2010; Haines et al. 2011a, 2011b, 2013), and the sSFRs of star-forming galaxies in infall regions are indistinguishable from those in coeval field samples (Haines et al. 2013). The colored curves show the predicted surface density profiles for quenching timescales t_Q in the range 0.25–10.0 Gyr. The best-fit model to observations has a quenching timescale $t_Q = 2.19 \pm 0.41$ Gyr, with a χ^2 value of 20.80 for 23 data points and two degrees of freedom (ϕ, t_Q).

5.3. Dynamical Analysis

The VDP of cluster galaxies, $\sigma_{\mathrm{los}}(r)$, provides complementary constraints for the accretion epochs of galaxy subpopulations (see Figure 13(d)). Figure 19 compares the observed VDPs of 24 μm-detected star-forming galaxies (blue points) with the predicted VDPs of model cluster galaxies, selected according to their accretion epoch.

The VDP for star-forming cluster galaxies shows a high, narrow peak of 1.44 σ_{ν} at $r_{\mathrm{proj}} \sim 0.3r_{500}$, before dropping to the innermost radial bin, and a steady decline outwards to $\sim$0.8 σ_{ν} at large radii. This profile shape is best reproduced by model cluster populations combining infalling galaxies yet to be accreted and the most recent arrivals into the cluster. The progressive inclusion of these recently accreted galaxies causes the velocity dispersion within r_{500} to rise rapidly, producing a characteristic sharp peak at $r_{\mathrm{proj}} \sim 0.2r_{500}$ which reaches a

maximum height of $\sim 1.56\,\sigma_\nu$ when $\Delta t = 0.7$ Gyr, along with a corresponding sharp drop off to the cluster core. The best overall match to observations is produced for models with $\Delta t \sim 0.5$–2.2 Gyr (light blue/green curves), comparable with the timescales required for infalling galaxies to approach the pericenter of their orbits through the cluster and achieve the high velocities required to produce the observed peak in $\sigma_{\rm los}(r)$. The observed profile is inconsistent with models with much longer delays between accretion into the cluster and quenching ($\Delta t \gtrsim 3.7$ Gyr), and models in which star formation is quenched instantaneously upon accretion ($\Delta t = 0$ Gyr; thick blue curve), due to their predicted low, relatively flat LOS VDPs within r_{500}.

The observed VDP considering all cluster members (black dashed curve) is not well matched by any model profile. While the predicted VDP considering all "spectroscopic" cluster galaxies peaks at $\sim 0.2 r_{500}$ and drops off sharply toward the cluster core (dark red curve), the observed VDP shows no corresponding dip in the cluster core. The $\sigma_{\rm los}(r)$ instead declines steadily from its peak value $1.18\,\sigma_\nu$ in the innermost radial bin, falling to values of $\sim 0.75\,\sigma_\nu$ over the range 1.6–$2.8 r_{500}$, significantly below the velocity dispersions predicted by simulations at these radii. Our observed VDP is qualitatively similar to that obtained by Rines et al. (2003) by stacking the member galaxies of eight $z < 0.05$ X-ray luminous clusters: their $\sigma_{\rm los}(r)$ also drops from $1.1\sigma_\nu$ in the cluster core to $0.8\,\sigma_\nu$ by r_{200}, albeit with marginal evidence for a decline within $0.1 r_{200}$. At larger radii ($\gtrsim 2 r_{500}$), their $\sigma_{\rm los}(r)$ drops to values of $\sim 0.5\,\sigma_\nu$, which is even lower than ours and hence poses further problems for the simulations.

One possible explanation is that the mismatch is linked to the prediction of too many model galaxies in the cluster core ($r_{\rm proj} \lesssim 0.1 r_{500}$; Figure 5), which assuming that the excess population were all accreted early, could artificially increase the contribution from low-velocity virialized cluster members, reducing the σ_ν estimates for each cluster, and pushing the resultant model curves upward.

Irrespective of the difficulties in reproducing the observed VDP of all cluster members, the key finding that the velocity dispersion of star-forming galaxies is 10%–35% higher than that of the overall cluster population at all radii, along with the apparent sharp peak in the VDP at $\sim 0.3 r_{500}$, unambiguously identifies the star-forming cluster galaxy population as recent arrivals. Considering a simple kinematical treatment of infalling and virialized cluster galaxies in a cluster-scale gravitational potential well leads to $|T/V| \approx 1$ for infalling galaxies and $|T/V| \approx 1/2$ for the virialized population, where T and V are the kinematic and potential energies. Thus, the velocity dispersions of the two populations are naively related by $\sigma_{\rm infall} \approx \sqrt{2}\,\sigma_{\rm virial}$ (Colless & Dunn 1996).

From the first dynamical studies of cluster galaxies, the velocity dispersions of spiral galaxies have been found to be systematically higher than early-types (Tammann 1972; Moss & Dickens 1977). Based on much larger samples, the stacked velocity dispersions of blue/emission-line galaxies were found to be 20% higher than the remaining inactive galaxies (Biviano et al. 1997; Aguerri et al. 2007). Biviano & Katgert (2004) showed that if early-type galaxies are assumed to have isotropic orbits within clusters, as supported by their Gaussian velocity distributions, the kinematic properties of late-type spirals are inconsistent with being isotropic at the >99% level. Instead they indicate that spirals and emission-line galaxies follow radial orbits in clusters, pointing toward many of them being on their first cluster infall.

Figure 7 showed the LOS velocity distribution of star-forming cluster galaxies within r_{500} to have a rather flat, top-hat profile, a high LOS velocity dispersion and a negative kurtosis ($\gamma_2 \sim -0.81$) strongly inconsistent with the Gaussian distribution typical of a virialized cluster population. This flat-topped distribution is well reproduced by model cluster galaxy populations that are either infalling into the cluster for the first time, or back-splash galaxies which are currently rebounding out of the cluster and are yet to reach apocenter (Figure 20). The velocity distributions of these two dynamical subpopulations appear indistinguishable within r_{500}, both having velocity dispersions $\sim 1.2\sigma_\nu$ and negative kurtosis values $\gamma_2 \sim -0.8$. At 1–$2 r_{500}$ the velocity distribution of star-forming galaxies becomes more rounded, albeit still with a negative kurtosis ($\gamma_2 \sim -0.6$), which again is well reproduced by the model infalling galaxy population ($\gamma_2 = -0.59$). At these radii, the back-splash population is expected to show a more Gaussian-like distribution with $\gamma_2 = -0.09$, inconsistent with observations. However, there are only expected to be 40% as many back-splash galaxies in this radial bin as infalling ones, and so we cannot rule out the possibility these star-forming galaxies represent a mixture of infalling and back-splash populations.

5.4. Distribution of Galaxies in the Caustic Diagram

The information gained from the galaxy surface density profiles and VDPs can be combined by comparing the observed spatial distribution of star-forming galaxies in the stacked caustic diagram (Figure 6) with those obtained from the Millennium simulation (Figure 13). Using the stacked sample of model galaxies from the 75 clusters extracted from the Millennium simulation, the distribution of model star-forming galaxies in the phase-space diagram $\Delta\nu_{\rm los}/\sigma_\nu$ versus $r_{\rm proj}/r_{500}$ was determined using the adaptive kernel estimator, for a range of quenching timescales from 0–10 Gyr.

As in Section 5.2 model star-forming cluster galaxies are given initial SFRs taken at random from our observed sample of coeval field star-forming galaxies (SFR $> 2\,M_\odot$ yr^{-1}; $0.15 < z < 0.30$). These are then set to decline exponentially on a quenching time t_Q once they pass within r_{200} of the cluster, until their SFRs fall below our nominal limit of $2.0\,M_\odot$ yr^{-1}. The redshift at which each model galaxy was accreted into the cluster is known, from which the number of quenching timescales t_Q passed between the epoch of accretion and the epoch of observation ($z = 0.21$) can be determined, and hence its final SFR and whether it would still be classified as star-forming. Those galaxies yet to be accreted are assumed to still be identified as star-forming. For each quenching timescale, t_Q, the spatial distribution of star-forming model galaxies in phase-space, $\rho(r_{\rm proj}/r_{500}, \Delta\nu_{\rm los}/\sigma_\nu)$, is determined using the adaptive Gaussian kernel method. Each model galaxy i is represented by a 2D Gaussian kernel of width $\sigma_0(\rho_i/\overline{\rho})^{-1/2}$, where $\overline{\rho}$ is the geometric mean of the local densities ρ_i of the model galaxies in phase-space, and σ_0 is the initial kernel width 0.2. To remove the effects of the discontinuity at $r_{\rm proj} = 0$, the phase-space distribution is mirrored about both velocity and radial axes. The distribution is normalized to unity when summed over the region $0.0 < (r_{\rm proj}/r_{500}) < 3.2$, so that it can be considered a probability distribution function, $P(r_{\rm proj}/r_{500}, \Delta\nu_{\rm los}/\sigma_\nu)$.

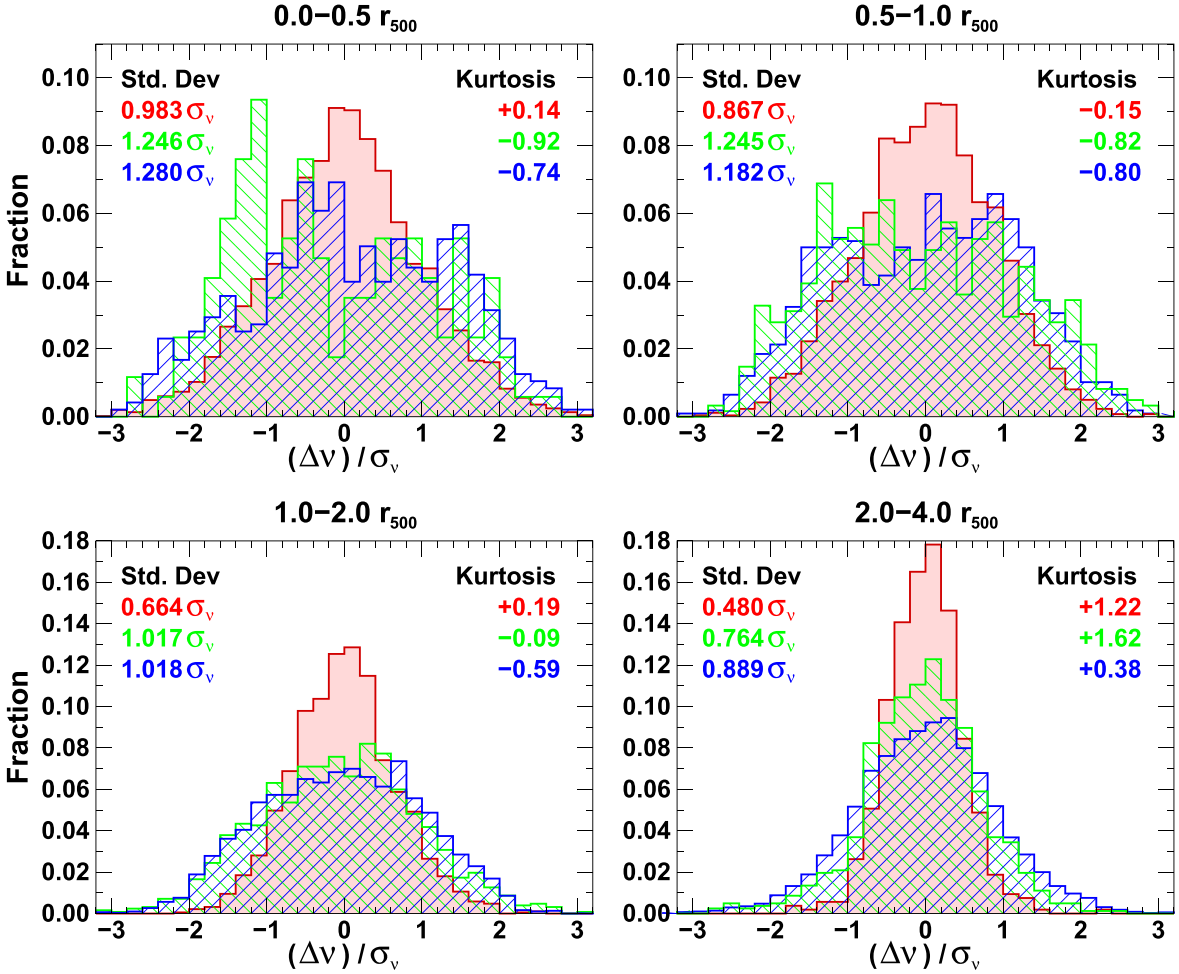

Figure 20. Stacked relative LOS velocity distributions of "spectroscopic" cluster galaxies for the 75 most massive clusters in the Millennium simulation at $z = 0.21$ split into three dynamic sub-populations: (i) infalling "spectroscopic" cluster members yet to reach pericenter (blue striped histogram); (ii) back-splash galaxies which have passed through pericenter, are on their way back out of the cluster $v_{\rm radial} > 0$, and are yet to reach apocenter (green striped histogram); and (iii) the virialized cluster population which has passed through apocenter (red solid histogram). Each panel represents a different bin in cluster-centric radius as in Figure 7. The standard deviations (in units of σ_v) and kurtosis values of each distribution are indicated.

The probability distributions of model star-forming galaxies for each value of t_Q are then compared with the observed distribution of star-forming galaxies in the stacked phase-space diagram (Figure 6). The best-fitting model cluster population is identified using a maximum-likelihood analysis, determining the value of t_Q for which the likelihood $\mathcal{L} = \prod_{i=1}^{N} P(r_{i,proj}/r_{500}, \Delta v_i/\sigma_v | t_Q)$ is maximized, taking into account corrections for spectroscopic incompleteness and radial variation in coverage by our 24 μm images as before.

Figure 21 displays the resulting likelihood function $\mathcal{L}(t_Q)$ as well as the 1, 2, and 3-σ confidence limits in t_Q. The closest match to the observed distribution of star-forming galaxies is obtained for a value of $t_Q = 1.73 \pm 0.25$ Gyr. Quenching timescales below 1 Gyr and above 3 Gyr are both excluded at $>3\sigma$ level, primarily due to the radial distribution of star-forming galaxies observed in our clusters (Figure 18).

Figure 22 shows the corresponding stacked caustic diagram of model star-forming cluster galaxies for $t_Q = 1.73$ Gyr. Each cluster galaxy is color-coded according to its accretion epoch, and the overall phase-space density distribution is shown by the grayscale contours. The model star-forming galaxies are most frequently found at large cluster-centric radii ($r_{\rm proj} \gtrsim 1.5 r_{500}$)

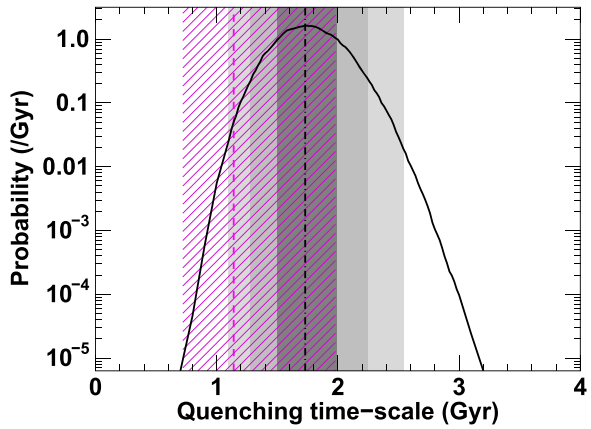

Figure 21. Likelihood function of the quenching timescale, t_Q, based on fitting the distribution of star-forming galaxies in the caustic diagram, normalized so that $\int \mathcal{L}(t_Q) = 1$ with t_Q in units of Gyr. The best-fit value of t_Q is indicated by the vertical dotted–dashed line, while the shaded regions indicate the 1, 2, and 3 σ confidence limits in t_Q. The magenta dashed line and hashed region indicates the best-fit t_Q value and 1 σ confidence limits by Haines et al. (2013) based on the systematically low sSFRs of star-forming cluster galaxies within r_{200}.

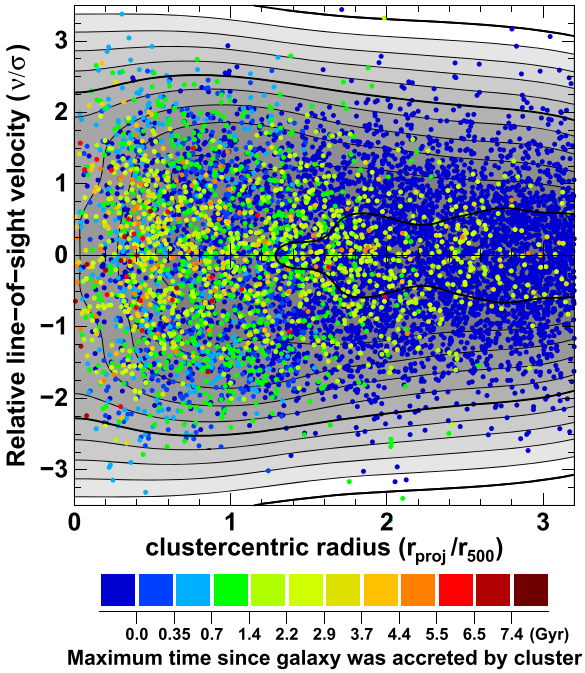

Figure 22. Stacked phase-space diagram, $\Delta v_z/\sigma_v$ vs. $r_{\rm proj}/r_{500}$, for model star-forming galaxies around the 75 most massive clusters in the Millennium simulation at $z = 0.21$ for the best-fit quenching model, in which star formation declines exponentially on a timescale $t_Q = 1.73$ Gyr in galaxies from the moment they pass within r_{200} of the cluster for the first time. Each point marks an $\mathcal{M} > 2 \times 10^{10}\,M_\odot$ star-forming galaxy with SFR $> 2.0 M_\odot$ yr^{-1}, colored according to time elapsed since it was accreted into the cluster (mid-blue if it is yet to be accreted). The grayscale contours indicate the resulting probability distribution function of the model star-forming galaxies in phase-space, P ($r_{\rm proj}/r_{500}$, $\Delta v_z/\sigma_v$). Each contour indicates a factor 0.2 dex change in phase-space density of model star-forming galaxies. The thick contours indicate a factor 10 change in phase-space density.

and low velocity offsets ($|\Delta v_{\rm los}| \lesssim 1.1\sigma_v$). The phase-space density of star-forming galaxies drops by a factor $\sim$3× as $r_{\rm proj}/r_{500} \to 0$, for $|\Delta v_{\rm los}| \lesssim 1.4\sigma_v$, producing the vertical contours in the left-center of the plot.

Averaging over the 75 simulated clusters, 42% of the model star-forming galaxies with $r_{\rm proj} < r_{200}$ and LOS velocities identifying them as "spectroscopic" cluster members are physically located outside r_{200} at the time of observation ($z = 0.21$) and have not been inside this radius at any time (mid-blue points), 33% have been accreted within the last Gyr (light blue/green points), 19% were accreted 1–3 Gyr ago, and just 6% were accreted >3 Gyr prior to observation. With the model SFRs declining exponentially upon accretion on a timescale of 1.73 Gyr, overall the model SFRs and sSFRs of the star-forming cluster galaxies ($r_{\rm proj} < r_{200}$) are reduced by 25% from their values prior to accretion, consistent with the systematic reduction of 28% in their sSFRs found in Haines et al. (2013).

6. DISCUSSION

We have shown via two independent methods that star formation in galaxies infalling into clusters is not extinguished immediately upon their arrival into the cluster, but requires a significant time of the order 1–3 Gyr to be quenched. First the steadily increasing surface density of star-forming galaxies toward the cluster core (Figure 18), as opposed to the flat radial profile predicted for instantaneous quenching models, simply requires star-forming galaxies to survive for a certain period within the cluster to build up the over-density seen in the cluster core, with a best-fit exponential quenching timescale $t_Q = 2.2 \pm 0.4$ Gyr. Second, the VDP of star-forming cluster galaxies is consistently 10%–35% higher than inactive cluster galaxies at all radii, rising up to a sharp peak of $1.44\sigma_v$ at $0.3r_{500}$, which is inconsistent with instantaneous quenching models, but similar to the predicted VDPs of models in which star-forming galaxies survive for 0.5–2.2 Gyr after being accreted (Figure 20). Combining both radial and velocity information, we compared the spatial distribution of star-forming galaxies within the caustic diagram with predictions from the Millennium simulation, to obtain a best-fit value of $t_Q = 1.73 \pm 0.25$ Gyr.

While these results robustly confirm that star-forming galaxies are able to continue forming stars for some significant period after being accreted into massive clusters, it is not possible simply based on the kinematics or distribution of star-forming galaxies within clusters to distinguish between slow quenching models whereby star formation declines exponentially (or linearly) over a long timescale, or a "delayed-then-rapid" quenching model in which recent arrivals continue to form stars normally for a certain period Δt, before suddenly stopping (Wetzel et al. 2012), as demonstrated by the similarity of the model curves in Figures 17 and 18.

6.1. The Slow Quenching of Star Formation in Cluster Galaxies

The key distinguishing feature of the "slow quenching" model is its impact on the distribution of SFRs or sSFRs among star-forming cluster galaxies, systematically lowering the mean sSFRs as a significant fraction of star-forming cluster galaxies are observed during this process of slow quenching, while the "delayed-then-rapid" quenching model leaves the sSFR distribution of star-forming cluster galaxies unchanged. Figure 8 supports the slow quenching model by finding kinematic segregation between star-forming cluster galaxies with normal or enhanced star formation, and those with *reduced* star formation, indicative of ongoing quenching. This suggests that the process of quenching occurs over a sufficiently long timescale that the kinematics and clustercentric radii of *quenching* star-forming galaxies to have evolved significantly. More definitively, in Haines et al. (2013) we found that the sSFRs of massive ($\gtrsim 10^{10} M_\odot$) star-forming cluster galaxies within r_{200} to be systematically 28% lower than their counterparts in the field at fixed stellar mass and redshift, a difference significant at the 8.7σ level. The entire sSFR distribution was seen to be shifted to lower values, marking the unambiguous signature of star formation in most (and possibly all) star-forming galaxies being *slowly* quenched upon their arrival into massive clusters. Assuming a model in which the SFRs decline exponentially upon passing within r_{200}, we obtained a best-fit quenching timescale of $1.17^{+0.81}_{-0.45}$ Gyr (magenta dashed line and hashed region in Figure 21), consistent with the timescales obtained here.

As well as skewing the sSFR distribution of cluster galaxies on or near the star-forming main sequence, the slow quenching model is expected to result in significant numbers of galaxies with sSFRs of $\sim 10^{-11}$ year^{-1} (or SFRs of 0.1–1 $M_\odot$ yr^{-1}), well below the sensitivity of our *Spitzer* data, and filling in the "green valley" gap between star-forming and passive galaxies. Wetzel et al. (2013) found no evidence of this large transition

population, leading them to prefer a delayed-then-rapid quenching model. One possible way of reconciling these two results would be a slow-then-rapid quenching model, whereby star formation is slowly quenched for the first 1–3 Gyr, to explain the results of Haines et al. (2013), followed-by a second short phase in which the residual star formation is rapidly terminated, in order to retain the observed bimodal sSFR distribution of satellite/cluster galaxies (Haines et al. 2011b; Wetzel et al. 2013).

Taranu et al. (2014) studied the bulge and disk colors of giant galaxies in $z \leqslant 0.1$ clusters, finding shallow, gradual radial trends in disk colors that could be reproduced by slow quenching models similar to our own, but requiring slightly longer timescales of $t_Q = 3$–3.5 Gyr. They ruled out short ($\lesssim$1Gyr) quenching timescales and "delayed-then-rapid" quenching models as both produced much larger and sharper radial changes in the median disk colors than observed. A number of other studies have also argued for relatively long timescales (∼1–4 Gyr) for the quenching of star formation in recently accreted cluster galaxies (Balogh et al. 2000; Moran et al. 2007; Finn et al. 2008; von der Linden et al. 2010; De Lucia et al. 2012; Wetzel et al. 2013).

Muzzin et al. (2014) found a population of post-starburst galaxies in nine $z \sim 1$ clusters, whose stacked spectrum could be fit by the rapid quenching ($t_Q = 0.4^{-0.3}_{-0.4}$ Gyr) of typical star-forming galaxies, and which traced a coherent "ring" at 0.25–$0.50r_{200}$ in the stacked caustic diagram that could be reproduced by recently accreted galaxies quenched 0.1–0.5 Gyr after passing within $0.5r_{200}$. This much more rapid quenching in high redshift clusters could be due to the shorter gas consumption timescales of galaxies at $z \sim 1$ (Carilli & Walter 2013) or ∼1.7× shorter cluster crossing timescales.

Slow quenching on ∼2 Gyr timescales matches predictions of starvation models, in which infalling galaxies are stripped of their diffuse gaseous halos as they pass through the ICM, preventing further gas accretion onto the galaxies from the surrounding inter-galactic medium (Larson et al. 1980; Bekki et al. 2002; McCarthy et al. 2008). The galaxy then slowly uses up its existing molecular and H I gas reservoir over a period of 2–3 Gyr, based on the gas consumption timescales observed for nearby spiral galaxies (Bigiel et al. 2011; Boselli et al 2014). This process may be effective well beyond the virial radius, with the extended gaseous halo of clusters remaining hot ($\gtrsim 10^6$ K) and sufficiently dense to strip the hot gas atmospheres of infalling galaxies out to $\sim 5r_{200}$ (Bahé et al. 2013; Gabor & Davé 2015).

Moreover, the growth of galactic DM halos is suppressed by tidal effects due to the presence of nearby cluster-mass halos (Hahn et al. 2009), which results in the peak mass of galactic halos infalling into clusters occurring at $\sim 1.8r_{\rm vir}$ ($3.5r_{500}$) on average (Behroozi et al. 2014). Given the tight correspondence between DM mass accretion and gas accretion onto galactic halos, including a significant fraction of gas accreted onto the galaxy via cold, dense filamentary streams at all redshifts (van de Voort et al. 2011), the radius of peak halo mass marks the end of continual gas replenishment of the ISM, signaling the beginning of the end for star formation in the host galaxy (Sánchez Almeida et al. 2014).

As these galaxies continue their journey toward the cluster core, the ICM they encounter becomes increasingly dense and the resultant ram pressures ($P_{\rm ram} \propto \rho_{\rm ICM} v^2$) become strong enough to progressively strip their gas disks from the outside in (Brüggen & de Lucia 2008), producing truncated H I, H_2 gas, and Hα disks (e.g., Koopmann & Kenney 2004; Boselli et al. 2006, 2014), and outer regions showing recently quenched stellar populations (Crowl & Kenney 2008). Hydrodynamical simulations predict that the moderate ram pressures acting on infalling massive spirals as they pass within $\sim r_{500} - r_{200}$ are sufficient to strip half their gas contents on 500–1000 Myr timescales (Roediger & Hensler 2005), while observations confirm that ram pressure stripping is effective at removing gas and quenching star formation as far out as r_{500} (Chung et al. 2007; Merluzzi et al. 2013). The effective timescale for quenching via ram-pressure stripping then becomes the ∼1 Gyr required for galaxies to travel from the cluster outskirts to the pericenter where the peak in ram pressure occurs (Roediger & Hensler 2005). The complete absence of H I-normal spirals within the r_{500} radius of Virgo and Coma clusters (Boselli & Gavazzi 2006), and the ∼0.5–0.8 dex H I deficiencies of Virgo spirals at fixed stellar mass, NUV−r color and stellar mass surface density, cannot be reproduced by predictions from chemospectrophotometric models involving starvation alone and can only be explained by ram-pressure stripping actively removing the gas (Cortese et al. 2011).

In typical spirals, the dust-to-gas ratio and internal extinction ($A_{\rm FUV}$) decline steadily with radius (Muñoz-Mateos et al. 2009), meaning that for ram pressure stripping events where gas is removed from the outside in, the more extended unobscured star formation component should be preferentially quenched prior to the more concentrated and bound obscured SF. This is supported by the finding of a significant cluster population of 24 μm-detected spirals with reduced SFRs, indicative of ongoing slow quenching, reddened by dust onto the optical red sequence (Wolf et al. 2009). This appears inconsistent with our finding that the quenching timescale for UV-selected star-forming cluster galaxies is ∼1 Gyr longer than that for 24 μm-selected galaxies. We suggest that the longer t_Q for the NUV-selected star-forming galaxies is due to the 1–1.5 Gyr timescale required for recently quenched galaxies to migrate from the blue cloud to red sequence in the (NUV–r) versus M_r C-M diagram (Kaviraj et al. 2007), while the 24 μm emission mostly originates from H II regions with ongoing star formation (e.g., Calzetti et al. 2005).

6.2. Pre-processing

In the SF-radius trends of Figures 2–4, the fraction of star-forming cluster galaxies rises steadily with radius, but crucially the $f_{\rm SF}(r)$ remain stubbornly 20%–30% below that seen in coeval field populations even out at $5r_{500}$, well beyond the maximal distances back-splash galaxies are expected to rebound to. As a result, these trends cannot be reproduced by models in which star formation is quenched in infalling galaxies via processes that are only initiated when they are accreted into the clusters (Figure 15). Our SF-radius trends are very similar to those of Chung et al. (2011), who analyzed 69 $z < 0.1$ clusters covered by both SDSS spectroscopy and *WISE*22 μm photometry, finding that the fraction of star-forming galaxies with $L_{\rm IR} > 4.7 \times 10^{10} L_\odot$ increases steadily with cluster-centric radius, but remains well below the field value even at $\sim 3r_{200}$. von der Linden et al. (2010) found that suppression of star formation in cluster galaxies could be traced out to $\sim 4r_{200}$. Wetzel et al. (2012) found their $f_{\rm SF}(r)$ suppressed with respect to field values as far out as $10r_{200}$

around cluster-mass halos ($M_{200} > 10^{14}\,M_{\odot}$), but interestingly saw this suppression entirely limited to satellite galaxies, with no evidence of suppression among centrals found beyond 1–2r_{200}.

The best way to reproduce the observed SF-radius trends appears to require a certain fraction of infalling galaxies to arrive onto the clusters having already been quenched (Figure 16). One commonly identified mechanism by which galaxies may be transformed at large distances from the cluster center is through "pre-processing" in infalling galaxy groups (e.g., Zabludoff et al. 1996; Zabludoff & Mulchaey 1998; Kodama et al. 2001; Fujita 2004; Berrier et al. 2009; McGee et al. 2009; Dressler et al. 2013). Star formation is suppressed in group galaxies, with $f_{\rm SF}$ values intermediate between those of field and cluster galaxy populations (Wilman et al. 2005; Bai et al. 2010; McGee et al. 2011; Rasmussen et al. 2012) up to at least $z \sim 1$ (Balogh et al. 2011; Ziparo et al. 2014). The fraction of star-forming galaxies within groups declines steadily with increasing group mass (at fixed stellar mass and group-centric distance) and proximity to the group center (Weinmann et al. 2006; Wetzel et al. 2012; Woo et al. 2013). The fractions and sSFRs of star-forming galaxies within groups both show *accelerated* declines since $z \sim 1$ with respect to the coeval field population (Popesso et al. 2015) and also "filament-like" environments with comparably high galaxy densities but no X-ray emission (Ziparo et al. 2014), indicative of ongoing slow quenching within groups (Balogh et al. 2011), comparable to that seen in our clusters (Haines et al. 2013). Galaxies in groups with masses $\gtrsim 10^{13}\,M_{\odot}$ are H I-deficient at fixed stellar mass and NUV−r color, suggesting that ram-pressure stripping can remove atomic gas from $\sim L^{*}$ spirals in such groups (Catinella et al. 2013).

Galaxy groups are ubiquitous, and host ∼50% of galaxies in the local universe (McGee et al. 2009). The impact of environmental quenching in groups will also be manifest in a reduced global fraction of star-forming galaxies in our coeval field sample. Hence, in order to reproduce the observation that the fraction of star-forming galaxies in the infall regions of clusters (2–3r_{200}) remains significantly lower than that seen in coeval field galaxies, a specific form of "pre-processing" is required, in which the galaxies infalling into clusters are *more likely* to be existing members of groups and hence *more likely* to be "pre-processed" than the cosmic average. That is we require the mass function of DM halos hosting galaxies in the surroundings of clusters (not including the cluster itself) to be top heavy and biased toward group-scale masses with respect to the cosmic average, as expected in such over-dense regions of the universe (Faltenbacher et al. 2010).

To examine this issue, we construct the mass function of the DM halos hosting galaxies at different cluster-centric radii and compare it with that of coeval field galaxies. We select galaxies within 4000 km s^{-1} of the mean redshifts of rich clusters ($M_{\rm halo} > 10^{14.2}\,M_{\odot}$) in the Millennium simulation at $z = 0.21$ (see Lu et al. 2012, for details), excluding those galaxies already accreted into the clusters. Figure 23 shows the resulting fractions of these model galaxies which reside in halos over a given mass as a function of projected cluster-centric radius (*solid curves*) for five values of minimum halo mass from $10^{12}\,M_{\odot}$ to $10^{14}\,M_{\odot}$. The dashed lines show the corresponding fractions for coeval field galaxies over the whole Millennium simulation. This confirms that galaxies infalling into clusters are indeed more likely to already reside within DM halos of a given mass than coeval field galaxies, for each halo mass range. While the effect is marginal for $10^{12}\,M_{\odot}$ mass halos, galaxies infalling into massive clusters are ∼35% more likely to already be residing in group-mass halos with $M_{\rm halo} > 10^{13}\,M_{\odot}$ and twice as likely to already be residing in $M_{\rm halo} > 10^{14}\,M_{\odot}$ halos than their counterparts in the field.

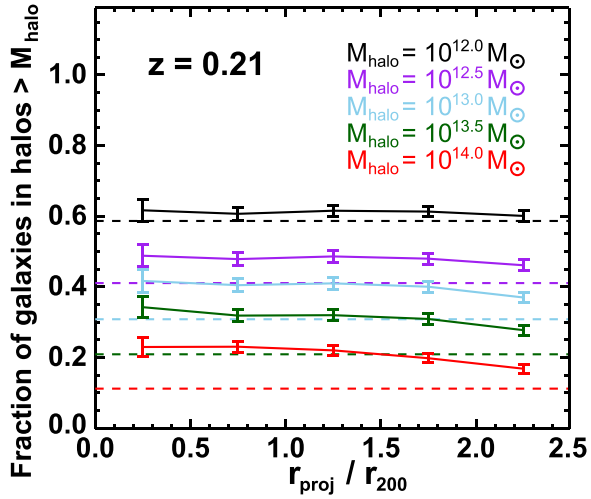

Figure 23. History bias for galaxies falling into massive clusters. The solid curves show the fraction of model galaxies surrounding massive clusters ($M_{\rm cl} > 10^{14.2}\,M_{\odot}$) at $z = 0.21$ which already reside in halos over a given mass as a function of projected cluster-centric radius. Only those galaxies yet to pass within r_{200} and be accreted into the cluster are included. The dashed curves show the corresponding cosmic fractions for field galaxies over the whole Millennium simulation.

We find numerous potential sites where infalling galaxies can be pre-processed before being accreted into the LoCuSS clusters (e.g., Pereira et al. 2010). Across the 23 clusters with *XMM* imaging, a total of 30 X-ray groups (with extended X-ray emission detected at >4σ levels) have been identified with redshifts placing them inside the cluster caustics, indicating that they are most likely infalling into the primary cluster (C. P. Haines et al. 2015, in preparation). Only six further "isolated" X-ray groups were detected (at >4σ) in the same *XMM* images over the rest of the 0.15–0.30 redshift range.

The observed ratio of ∼5 X-ray groups associated with the clusters for every field X-ray group in the remainder of the $0.15 < z < 0.30$ volume covered by *XMM*, is double (quadruple) the ratio obtained for cluster and field $M_K < M_K^{*} + 1.5$ (24 μm-detected) galaxies in the same two volumes. This suggests that infalling galaxies are 2–4 × more likely to be members of X-ray groups than in typical field regions, assuming that both group samples have similar numbers of members per group.

A second factor in the shortfall in $f_{\rm SF}$ at large radii could arise from a bias in the mass assembly history of the infalling galaxies and groups themselves. Maulbetsch et al. (2007) find that galactic $\sim 10^{12}\,M_{\odot}$ halos in high-density regions, such as the infall regions of massive clusters, form earlier, have more active merger histories, and have much lower mass accretion rates (and commensurate gas accretion rates; van de Voort et al. 2011) at late epochs ($z \lesssim 0.5$) than those which form in low-density field environments. Such halos in high-density regions are ∼4 × likelier to not be accreting any mass

(or even losing it) at late epochs than those in low-density regions.

7. SUMMARY

We present an analysis of the radial distribution and kinematics of star-forming galaxies in 30 massive clusters at $0.15 < z < 0.30$, combining wide-field *Spitzer* 24 μm and *GALEX* NUV photometry with highly complete spectroscopy of cluster members. To gain insights into how the observed trends relate to the continual accretion of star-forming spirals onto massive clusters and subsequent quenching of star formation, we follow the infall and orbits of galaxies in the vicinity of the 75 most massive clusters in the Millennium cosmological simulation, obtaining a series of predicted model trends that should have general applicability for understanding galaxy evolution in cluster environments. Our main results are summarized below.

1. The surface density of star-forming galaxies declines steadily with radius, falling ∼15× from the cluster core to $2r_{200}$. This simple observation requires star formation to survive within recently accreted spirals for 2–3 Gyr to build up the apparent over-density of star-forming galaxies within clusters.
2. The VDP of the star-forming cluster galaxy population shows a sharp peak of 1.44 σ_ν at $0.3r_{500}$, and is 10%–35% higher than that of the inactive cluster members at all cluster-centric radii, while their velocity distributions show a flat, top-hat profile within r_{500}. All of these results are consistent with star-forming cluster galaxies being an infalling population, but one that must also survive ∼0.5–2 Gyr beyond passing within r_{200} to achieve the high observed velocities.
3. The distributions of star-forming galaxies in the stacked caustic diagram are best-fit by models in which their SFRs decline exponentially on quenching timescales $t_Q = 1.73 \pm 0.25$ Gyr upon accretion into the cluster. The above results, and the observed kinematic segregation of star-forming galaxies according to their sSFRs, support the conclusion from Haines et al. (2013) that star formation in most (and possibly all) high-mass star-forming galaxies is *slowly* quenched on accretion into rich clusters on 0.7–2.0 Gyr timescales
4. The fraction (f_{SF}) of star-forming cluster galaxies rises steadily with cluster-centric radius, increasing five-fold by $2r_{200}$, but remains well below field values even at $3r_{200}$. Pre-processing in infalling galaxy groups appears to be the most likely explanation for this suppression of star formation at large distances from the cluster.

C.P.H. was funded by CONICYT Anillo project ACT-1122. G.P.S. acknowledges support from the Royal Society. F.Z. and G.P.S. acknowledge support from the Science and Technology Facilities Council. We acknowledge NASA funding for this project under the *Spitzer* program GO:40872. This work was supported in part by the National Science Foundation under grant No. AST-1211349. The Millennium simulation databases used in this paper and the web application providing online access to them were constructed as part of the activities of the German Astrophysical Virtual Observatory.

REFERENCES

Aguerri, J. A. L., Sánchez-Janssen, R., & Muñoz-Tuñón, C. 2007, A&A, 471, 17
Ascasibar, Y., & Diego, J. M. 2008, MNRAS, 383, 369
Bahé, Y. M., McCarthy, I. G., Balogh, M. L., & Font, A. S. 2013, MNRAS, 430, 3017
Bai, L., Rasmussen, J., Mulchaey, J. S., et al. 2010, ApJ, 713, 637
Balogh, M. L., Eke, V., Miller, C., et al. 2004, MNRAS, 348, 1355
Balogh, M. L., McGee, S. L., Wilman, D. J., et al. 2011, MNRAS, 412, 2303
Balogh, M. L., Navarro, J. F., & Morris, S. L. 2000, ApJ, 540, 113
Beers, T. C., Flynn, K., & Gebhardt, K. 1990, AJ, 100, 32
Behroozi, P. S., Wechsler, R. H., Lu, Y., et al. 2014, ApJ, 787, 156
Bekki, K., Couch, W. J., & Shioya, Y. 2002, ApJ, 577, 651
Bell, E. F., McIntosh, D. H., Katz, N., & Weinberg, M. D. 2003, ApJS, 149, 289
Berrier, J. C., Stewart, K. R., Bullock, J. S., Purcell, C. W., & Barton, E. J. 2009, ApJ, 690, 1292
Bertin, E., & Arnouts, S. 1996, A&AS, 117, 393
Bigiel, F., Leroy, A. K., Walter, F., et al. 2011, ApJL, 730, L13
Binggeli, B., Tammann, G. A., & Sandage, A. 1987, AJ, 94, 251
Biviano, A., & Katgert, P. 2004, A&A, 424, 779
Biviano, A., Katgert, P., Mazure, A., et al. 1997, A&A, 321, 84
Biviano, A., Rosati, P., Balestra, I., et al. 2013, A&A, 558, 1
Böhringer, H., Schuecker, P., Guzzo, L., et al. 2004, A&A, 425, 367
Boselli, A., Boissier, S., Cortese, L., et al. 2006, ApJ, 651, 811
Boselli, A., Cortese, L., Boquien, M., et al. 2014, A&A, 564, 67
Boselli, A., & Gavazzi, G. 2006, PASP, 118, 517
Bower, R. G., Benson, A. J., Malbon, R., et al. 2006, MNRAS, 370, 645
Boylan-Kolchin, M., Springel, V., White, S. D. M., Jenkins, A., & Lemson, G. 2009, MNRAS, 398, 1150
Bressan, A., Panuzzo, P., Buson, L., et al. 2006, ApJL, 639, L55
Brüggen, M., & de Lucia, G. 2008, MNRAS, 383, 1336
Budzynski, J. M., Koposov, S. E., McCarthy, I. G., McGee, S. L., & Belokurov, V. 2012, MNRAS, 423, 104
Calzetti, D., Kennicutt, R. C. Jr., Bianchi, L., et al. 2005, ApJ, 633, 871
Carilli, C. L., & Walter, F. 2013, ARA&A, 51, 105
Catinella, B., Schiminovich, D., Cortese, L., et al. 2013, MNRAS, 436, 34
Chabrier, G. 2003, PASP, 115, 763
Chilingarian, I. V., Melchior, A.-L., & Zolotukhin, I. Y. 2010, MNRAS, 405, 1409
Chung, A., van Gorkom, J. H., Kenney, J. D. P., & Vollmer, B. 2007, ApJL, 659, L115
Chung, S. M., Eisenhardt, P. R., Gonzalez, A. H., et al. 2011, ApJ, 743, 34
Clemens, M. S., Bressan, A., Panuzzo, P., et al. 2009, MNRAS, 392, 982
Colless, M., & Dunn, A. M. 1996, ApJ, 458, 435
Cortese, L., Catinella, B., Boissier, S., Boselli, A., & Heinis, S. 2011, MNRAS, 415, 1797
Crowl, H. H., & Kenney, J. D. P. 2008, AJ, 136, 1623
Dale, D. A., Aniano, G., Engelbracht, C. W., et al. 2012, ApJ, 745, 95
De Lucia, G., & Blaizot, J. 2007, MNRAS, 375, 2
De Lucia, G., Weinmann, S., Poggianti, B. M., Aragón-Salamanca, A., & Zaritsky, D. 2012, MNRAS, 423, 1277
Diaferio, A., Kauffmann, G., Balogh, M. L., et al. 2001, MNRAS, 323, 999
Diaferio, A. 1999, MNRAS, 309, 610
Diaferio, A., & Geller, M. J. 1997, ApJ, 481, 68
Dressler, A., Oemler, A., Jr., Fritz, J., et al. 2013, ApJ, 770, 62
Dünner, R., Reisenegger, A., Meza, A., Araya, P. A., & Quintana, H. 2007, MNRAS, 376, 1577
Ellingson, E., Lin, H., Yee, H. K. C., & Carlberg, R. G. 2001, ApJ, 547, 609
Faltenbacher, A., Finoguenov, A., & Drory, N. 2010, ApJ, 712, 484
Finn, R. A., Balogh, M. L., Zarizsky, D., Miller, C. J., & Nichol, R. C. 2008, ApJ, 679, 279
Finn, R. A., Desai, V., Rudnick, G., et al. 2010, ApJ, 720, 87
Finoguenov, A., Connelly, J. L., Parker, L. C., et al. 2009, ApJ, 704, 564
Frenk, C. S., White, S. D. M., Bode, P., et al. 1999, ApJ, 525, 554
Fujita, Y. 2004, PASJ, 56, 29
Gabor, J. M., & Davé, R. 2015, MNRAS, 447, 37
Gao, L., Navarro, J. F., Frenk, C. S., et al. 2012, MNRAS, 425, 2169
Gao, L., White, S. D. M., Jenkins, A., Stoehr, F., & Springel, V. 2004, MNRAS, 355, 819
Gehrels, N. 1986, ApJ, 303, 336
Geller, M. J., Hwang, H. S., Diaferio, A., et al. 2014, ApJ, 784, 52
Gifford, D., Miller, C., & Kern, N. 2013, ApJ, 773, 116
Giles, P. A., Maughan, B. J., Birkinshaw, M., Worrall, D. M., & Lancaster, K. 2012, MNRAS, 419, 503

Gill, S. P. D., Knebe, A., & Gibson, B. K. 2005, MNRAS, 356, 1327
Guo, Q., White, S., Boylan-Kolchin, M., et al. 2011, MNRAS, 413, 101
Hahn, O., Porciani, C., Dekel, A., & Carollo, C. M. 2009, MNRAS, 398, 1742
Haines, C. P., Gargiulo, A., la Barbera, F., et al. 2007, MNRAS, 381, 7
Haines, C. P., Gargiulo, A., & Merluzzi, P. 2008, MNRAS, 385, 1201
Haines, C. P., Smith, G. P., Egami, E., et al. 2009, ApJ, 704, 126
Haines, C. P., Smith, G. P., Pereira, M. J., et al. 2010, A&A, 518, L19
Haines, C. P., Busarello, G., Merluzzi, P., et al. 2011a, MNRAS, 412, 127
Haines, C. P., Busarello, G., Merluzzi, P., et al. 2011b, MNRAS, 412, 145
Haines, C. P., Pereira, M. J., Sanderson, A. J. R., et al. 2012, ApJ, 754, 97
Haines, C. P., Pereira, M. J., Smith, G. P., et al. 2013, ApJ, 775, 126
Hernández-Fernández, J. D., Haines, C. P., Diaferio, A., et al. 2014, MNRAS, 438, 2186
Jaffé, Y. L., Smith, R., Candlish, G. N., et al. 2015, MNRAS, 448, 1715
Kaviraj, S., Kirkby, L. A., Silk, J., & Sarzi, M. 2007, MNRAS, 382, 960
Kennicutt, R. C., Jr. 1983, AJ, 88, 483
Kodama, T., Smail, I., Nakata, F., Okamura, S., & Bower, R. G. 2001, ApJL, 562, L9
Koopmann, R. A., & Kenney, J. D. P. 2004, ApJ, 613, 866
Kroupa, P. 2002, Sci, 295, 82
Larson, R. B., Tinsley, B. M., & Caldwell, C. N. 1980, MNRAS, 237, 692
Lewis, I., Balogh, M., De Propris, R., et al. 2002, MNRAS, 334, 673
Lin, Y.-T., & Mohr, J. J. 2004, ApJ, 617, 879
Lin, Y.-T., Mohr, J. J., & Stanford, S. A. 2004, ApJ, 610, 745
Lu, T., Gilbank, D. G., McGee, S. L., Balogh, M. L., & Gallagher, S. 2012, MNRAS, 420, 126
Mahajan, S., Mamon, G. A., & Raychaudhury, S. 2011, MNRAS, 416, 2882
Mamon, G. A., Biviano, A., & Murante, G. 2010, A&A, 520, 30
Mamon, G. A., Sanchis, T., Salvador-Solé, E., & Solanes, J. M. 2004, A&A, 414, 445
Martino, R., Mazzotta, P., Bourdin, H., et al. 2014, MNRAS, 443, 2342
Maulbetsch, C., Avila-Reese, V., Colín, P., et al. 2007, ApJ, 654, 53
McCarthy, I. G., Frenk, C. S., Font, A. S., et al. 2009, MNRAS, 383, 593
McGee, S. L., Balogh, M. L., Bower, R. G., Font, A. S., & McCarthy, I. G. 2009, MNRAS, 400, 937
McGee, S. L., Balogh, M. L., Wilman, D. J., et al. 2011, MNRAS, 413, 996
Mercurio, A., Girardi, M., Boschin, W., Merluzzi, P., & Busarello, G. 2003, A&A, 397, 431
Merluzzi, P., Busarello, G., Dopita, M. A., et al. 2013, MNRAS, 429, 1747
Moran, S. M., Ellis, R. S., Treu, T., et al. 2007, ApJ, 671, 1503
Moss, C., & Dickens, R. J. 1977, MNRAS, 178, 701
Muñoz-Mateos, J. C., Gil de Paz, A., Boissier, S., et al. 2009, ApJ, 701, 1965
Muzzin, A., Yee, H. K. C., Hall, P. B., Ellingson, E., & Lin, H. 2007, ApJ, 659, 1106
Muzzin, A., van de Burg, R. F. J., McGee, S. L., et al. 2014, ApJ, 796, 65
Navarro, J. F., Frenk, C. S., & White, S. D. M. 1997, ApJ, 490, 493
Norberg, P., Cole, S., Baugh, C. M., et al. 2002, MNRAS, 336, 907
Okabe, N., Smith, G. P., Umetsu, K., Takada, M., & Futamase, T. 2013, ApJL, 769, L35
Okabe, N., Takada, M., Umetsu, K., Futamase, T., & Smith, G. P. 2010, PASJ, 62, 811
Owers, M. S., Nulsen, P. E. J., & Couch, W. J. 2011, ApJ, 741, 122
Peng, Y., Lilly, S. J., Kovac, K., et al. 2010, ApJ, 721, 193
Peng, Y., Lilly, S. J., Renzini, A., & Carollo, M. 2012, ApJ, 757, 4
Pereira, M. J., Haines, C. P., Smith, G. P., et al. 2010, A&A, 518, L40
Piovan, L., Tantalo, R., & Chiosi, C. 2003, A&A, 408, 559
Popesso, P., et al. 2014, arXiv:1407.8214
Popesso, P., Biviano, A., Finoguenov, A., et al. 2015, A&A, 574, 105
Rasmussen, J., Mulchaey, J. S., Lei, B., et al. 2012, ApJ, 757, 122
Rawle, T. D., Edge, A. C., Egami, E., et al. 2012, ApJ, 747, 29
Rieke, G. H., Young, E. T., Engelbracht, C. W., et al. 2004, ApJS, 154, 25
Rieke, G. H., Alonso-Herrero, A., Weiner, B. J., et al. 2009, ApJ, 556
Rines, K., & Diaferio, A. 2006, AJ, 132, 1275
Rines, K., Geller, M. J., Diaferio, A., & Kurtz, M. J. 2013, ApJ, 767, 15
Rines, K., Geller, M. J., Kurtz, M. J., & Diaferio, A. 2003, AJ, 126, 2152
Roediger, E., & Hensler, G. 2005, A&A, 433, 875
Salim, S., & Rich, R. M. 2010, ApJL, 714, 290
Sánchez Almeida, J., Elmegreen, B. G., Muñoz-Tuñón, C., & Elmegreen, D. M. 2014, A&ARv, 22, 71
Sanderson, A. J. R., Edge, A. C., & Smith, G. P. 2009, MNRAS, 398, 1698
Sanderson, A. J. R., & Ponman, T. J. 2010, MNRAS, 402, 65
Sanderson, A. J. R., & Ponman, T. J. 2003, MNRAS, 345, 1241
Serra, A. L., Diaferio, A., Murante, G., & Borgani, S. 2011, MNRAS, 412, 800
Smith, G. P., Khosroshahi, H. G., Dariush, A., et al. 2010a, MNRAS, 409, 169
Smith, G. P., Haines, C. P., Pereira, M. J., et al. 2010b, A&A, 518, L18
Springel, V., White, S. D. M., Jenkins, A., et al. 2005, Natur, 435, 629
Tammann, G. A. 1972, A&A, 21, 355
Taranu, D. S., Hudson, M. J., Balogh, M. L., et al. 2014, MNRAS, 440, 1934
van de Voort, F., Schaye, J., Booth, C. M., Haas, M. R., & Dalla Vecchia, C. 2011, MNRAS, 414, 2458
Vogelsberger, M., Genel, S., Springel, V., et al. 2014, Natur, 509, 177
von der Linden, A., Wild, V., Kauffmann, G., White, S. D. M., & Weinmann, S. 2010, MNRAS, 404, 1231
Weinmann, S. M., Kauffmann, G., von der Linden, A., & de Lucia, G. 2010, MNRAS, 406, 2249
Weinmann, S. M., van den Bosch, F. C., Yang, X., & Mo, H. J. 2006, MNRAS, 366, 2
Wetzel, A. R., Tinker, J. L., & Conroy, C. 2012, MNRAS, 424, 232
Wetzel, A. R., Tinker, J. L., Conroy, C., & van den Bosch, F. 2013, MNRAS, 432, 336
Wijesinghe, D. B., Hopkins, A. M., Brough, S., et al. 2012, MNRAS, 423, 3679
Wilman, D. J., Balogh, M. L., Bower, R. G., et al. 2005, MNRAS, 358, 88
Wolf, C., Aragón-Salamanca, A., Balogh, M., et al. 2009, MNRAS, 393, 1302
Woo, J., Dekel, A., Faber, S. M., et al. 2013, MNRAS, 428, 3306
Wyder, T. K., Martin, D. C., Schiminovich, D., et al. 2007, ApJS, 173, 293
Xu, L., Rieke, G. H., Egami, E., et al. 2015, ApJ, in press
Zabludoff, A. I., & Mulchaey, J. S. 1998, ApJ, 496, 39
Zabludoff, A. I., Zaritsky, D., Lin, H., et al. 1996, ApJ, 466, 104
Ziparo, F., Popesso, P., Finoguenov, A., et al. 2014, MNRAS, 437, 458